

# CubeSat De-Orbit Point Targeting using Drag Modulations

a project presented to  
The Faculty of the Department of Aerospace Engineering  
San José State University

in partial fulfillment of the requirements for the degree  
*Master of Science in Aerospace Engineering*

by

**Sebastian Smith**

December 2017

approved by

Dr. Marcus Murbach  
Faculty Advisor



# CubeSat De-Orbit Point Targeting using Drag Modulations

Sebastian Smith \*

Marcus Murbach †

## Abstract

Spacecraft de-orbit point targeting can be used for quick returns from low Earth orbits by relying solely on a passive drag device. Using a series of drag modulations, a small satellite can target a pre-selected terminal location provided that the targets' latitude is less than the orbit inclination and that initial altitude meets specific criteria. Utilizing an Exo-Brake, a passive drag device capable of manipulating its reference area, orbital decay rates can be compared to analyze its effectiveness at various altitudes. A numerical propagator using the Jacchia Bowman 2008 atmospheric model was developed in MATLAB to predict the trajectory and the total amount of time until re-entry. The initial trajectory can then be used as a reference point to determine the proper ballistic profile necessary for reaching the desired target. In this paper, multiple target sites and initial condition constraints were used to assess the accuracy of the model. A targeting error of 100 km was chosen to allow for the final stage, a guided parafoil, to steer the satellite remains to the desired location. While it is possible to obtain a targeting error under 100 km using drag modulation techniques, other control methods should be considered to provide a more robust and accurate solution.

*Keywords:* Orbit-Decay, Aerodynamic Drag, Exo-Brake, Drag Modulation, MATLAB, TechEdSat, NASA Ames Research Center, Re-entry targeting, De-Orbit Propagator

## Nomenclature

- $\omega$  Argument of perigee (km)
- $h$  Angular momentum of the spacecraft
- $J_2$  Orbit perturbations due to planet oblatness

---

\*Masters Student, Department of Aerospace Engineering, SJSU

†Principal Investigator, NASA Ames Research Center, SJSU Advisor

|                     |  |
|---------------------|--|
| $R_{Earth}$         | Radius of the Earth (km)   |
| $a_{drag}$          | acceleration due to atmospheric drag ( $\frac{km}{s}$ )  |
| $C_D$               | Drag coefficient   |
| A                   | Reference Area ( $m^2$ )   |
| m                   | Mass (kg)  |
| $\rho$              | Density ( $\frac{kg}{m^3}$ )   |
| $v_{sat}$           | Velocity relative to the spacecraft ( $\frac{km}{s}$ )   |
| r                   | Radius from the center of the planet to the center of the satellite (km)                       |
| $v_{atm}$           | Velocity relative to the atmosphere ( $\frac{km}{s}$ )   |
| $\beta$             | Ballistic coefficient ( $\frac{kg}{m^2}$ )   |
| $T_g$               | Gravity gradient torque ( $\frac{N}{km}$ )   |
| I                   | Moment of inertia  |
| $\lambda$           | Mean longitude (deg)   |
| $M_e$               | Mean anomaly of elliptical or circular orbit (rad)   |
| E                   | Eccentric anomaly (rad)  |
| M                   | Mean motion ( $\frac{rad}{s}$ )  |
| $\Delta\theta_d$    | Difference in total change in true anomaly between the new and old trajectory (rad)            |
| $\Delta t$          | Time until swap point in the new trajectory (s)  |
| p                   | Semi-latus rectum (km)   |
| $\Delta t$          | Time from swap point until terminal point in the new trajectory                                |
| $\Delta t_{10}$     | Time until swap point in the initial trajectory (s)  |
| $\Delta t_{20}$     | Time from swap point until terminal point in the initial trajectory (s)                        |
| $\Delta\theta_{10}$ | Change in true anomaly from the initial time to the swap time in the initial trajectory (rad)  |
| $\Delta\theta_t$    | Desired total change in true anomaly of the new trajectory until the terminal location         |
| $\Delta\theta_{20}$ | Change in true anomaly from the swap time to the terminal time in the initial trajectory (rad) |

|                  |  |
|------------------|--|
| $\Delta\theta_1$ | Change in true anomaly from the initial time to the swap time in the new trajectory (rad)  |
| $\Delta\theta_2$ | Change in true anomaly from the swap time to the terminal time in the new trajectory (rad) |
| $\Delta t_t$     | Total time for the new trajectory to reach the terminal location (s)                       |
| $\Delta\theta_d$ | Difference in total change in true anomaly between initial and new trajectories (rad)      |
| $e$              | eccentricity of the orbit  |
| $\theta$         | True anomaly   |
| $T$              | Orbital Period (s)   |
| $\mu$            | Gravitational Constant ( $\frac{m^3}{kg\ s^2}$ )   |
| $a$              | Semi-major axis (km)   |
| $i$              | Orbit inclination (rad)  |
| $\Omega$         | Right ascension of the ascending node (rad)  |

## 1 Introduction

The ability to frequently return payloads from low Earth orbit has become increasingly popular since the retirement of the Space Shuttle program in 2011. While re-entry devices such as NASA's Orion spacecraft and SpaceX's Dragon capsule have the ability to return large amounts of cargo, factors such as cost of deployment and infrequent launch dates make them impractical for smaller payloads onboard the ISS. Under the Small Payload Quick Return (SPQR) and Sub Orbital Aerodynamic Re-entry EXperiments (SOAREX) projects, NASA proposes to test a series of small satellites aimed to fill the demand for smaller payloads utilizing an Exo-Brake, a parachute-like, modulating drag device capable of changing its reference area to produce drag in exoatmospheric conditions. The TechEdSat series, a line of CubeSat's ranging from 1U-6U, is the primary test-bed for the Exo-Brake design and deployment. In addition to quick returns, the Exo-Brake offers the unique ability to target a re-entry location without any propulsive devices, so as long as the desired target lies on the given orbit path. Guaranteeing a safe and controlled re-entry becomes crucial to mission planning as some of the satellite, including the payload, will eventually have components capable of surviving the re-entry process, posing as a potential threat to the surrounding inhabitants.

TechEdSat, or Technology Educational Satellite, is a series of low-cost CubeSats designed to test new technologies in satellite-to-satellite communications and passive de-orbiting. Beginning as a conjoined project between San Jose State University, Sweden's ÅAC Microtec, and NASA Ames Research Center in 2012, the original TES was engineered to evaluate plug-and-play

avionics and experiment with orbital communications using Iridium and Orbcomm satellite phone networks. TechEdSat-3p, launched in November 2013, then became the first flight test with the Exo-Brake passive de-orbit system, marking the beginning of quick return experiments designed for ISS and Mars re-entry applications. Taking up roughly 2/3 of the total volume, the erectable deployment system was engineered as a tension-based structure to help the spacecraft re-enter in 10 days after being deployed from the space station. Building upon the Exo-Brake design, TechEdSat 5 added the ability to modulate the surface area to allow more precise atmospheric entry predictions. Utilizing a single winch system, the Exo-Brake's canopy can be extended or retracted, effectively changing the reference area to modulate drag. With upcoming launches planned for the fall of 2017 and 2018, future TechEdSat's look to further expand the development of the Exo-Brake. While the eventual goal is to fully target and control the spacecraft autonomously, initial tests will control the Exo-Brake via Iridium constellation to validate the control algorithm and confirm that guided re-entry is possible using only an Exo-Brake.



Figure 1: TechEdSat 1 (far left) being deployed in 2012 [9]

## 2 Orbital Mechanics for a Two-Body Problem

In order to understand the optimal trajectory for TechEdSat's guided de-orbit, basic orbital mechanics based off Kepler's laws and their corresponding orbital elements must be first considered for an initially circular orbit. The classical two-body problem is defined when two bodies' motion can be determined solely by their own mutual gravitational attraction.

### 2.1 Kepler's Laws

The three laws that describe the motion of planets around the Sun are known as Kepler's laws.

1. The orbit of a planet is an ellipse with the Sun at one of the two foci.

$$r = \frac{p}{1 + e \cos(\theta)} \quad (1)$$

2. A line segment from the center of the sun to the center of the planet will sweep out in equal areas over an equal interval of time.

$$\frac{dA}{dt} = \frac{1}{2} r^2 \frac{d\theta}{dt} \quad (2)$$

3. The square of a planets orbital period is proportional to the cube of the of the semi-major axis of its orbit.

$$\frac{T^2}{r^3} = \frac{4\pi^2}{\mu} \quad (3)$$

Kepler's first law, also known as the law of ellipses, states that all the planets orbiting the sun follow an elliptical path with the sun at one of the foci. Equation 1 shows the relationship of radius with the semi-latus rectum, eccentricity, and true anomaly. The second law, or the law of equal areas, describes the speed of a planet while it orbits the Sun. Because a planets velocity varies proportionally to its distance from the Sun, the velocity will vary along the orbits path. Despite the speed of the planet, Kepler's second law states that in equal times, the object will sweep equal areas for that orbit. Unlike Kepler's second law, the third law, or the law of harmonics, compares the orbital periods and radi of multiple planets. This relationship between orbital period and radius offer insight to the fundamental principles of motion for both satellites and planets. [2, 6]

## 2.2 Keplerian Elements

The basis of orbital mechanics revolve around Kepler's three laws of planetary motion and the elements that govern them. Keplerian elements describe the orbit of an object, such as a satellite, around a large body using the following parameters:

1.  $a$ , Semi-Major Axis: The distance between perigee and the center of the orbit
2.  $e$ , Eccentricity: The ratio of half the foci separation to the semi-major axis
3.  $i$ , Inclination: The angle between the equatorial plane and the orbital plane, measured counterclockwise at the ascending node
4.  $\Omega$ , Right Ascension of the Ascending Node: The angle between the vernal equinox to the ascending node
5.  $\omega$ , Argument of perigee: The angle measured from the ascending node to the perigee
6.  $\theta$ , True Anomaly: The angle measured from perigee to the satellites location

Each Keplerian element is designed to describe a unique aspect of the objects motion. The semi-major axis is used to describe the orbits size while the eccentricity and inclination elements portray the orbits shape and plane tilt respectively.  $\Omega$ ,  $\omega$ , and  $\theta$  each describe the orbital planes rotation about the Earth, the orbits orientation in the orbital plane, and the satellites location within the orbit respectively. Keplerian elements can then be expressed in a set called a TLE, or two-line element. TLE's compact orbital elements of an Earth-orbiting object for a given time and represent the trajectory of the spacecraft in two lines of 80-column ASCII text. [2, 6]

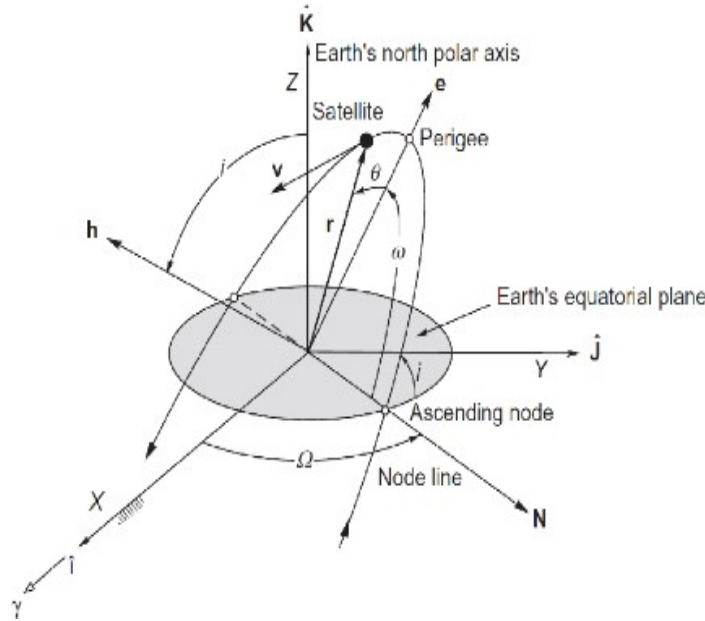


Figure 2: Keplerian Elements using a Geocentric Equatorial Frame [2]

### 2.3 Governing Equations

For determining the motion of two bodies based solely off their mutual gravitational attraction, the path of one of the masses relative to the other resembles a conic section whose shape is determined by the eccentricity of the orbit. The equation that describes this two-body orbit is known as the orbit equation.

$$r = \frac{h^2}{\mu} \frac{1}{1 + e \cos(\theta)} \quad (4)$$

where,

$$\mathbf{h} = \mathbf{r} \times \dot{\mathbf{r}} \quad (5)$$

For a two-body orbit, or Keplerian orbit,  $\mu$ ,  $h$ , and  $e$  are all constants. Because the orbit equation models conic sections, it becomes a mathematical expression of Kepler's first law. When the eccentricity is equal to zero, then the orbit is said to be circular. Because the orbit is a circle,  $r$  becomes a constant and therefore the radial velocity,  $\dot{r}$  is zero. For this unique

situation, the position and velocity vectors can be shown as follows:

$$r = \frac{h^2}{\mu} \quad (6)$$

$$v = \frac{\mu}{r} \quad (7)$$

In addition, the acceleration of a satellite in a circular orbit about the Earth for a basic two body problem can be expressed by the following equation:

$$\ddot{r} = -\frac{\mu}{r^3} r \quad (8)$$

$$(9)$$

where,

$$r = x + y + z \quad \text{and} \quad r = \sqrt{x^2 + y^2 + z^2} \quad (10)$$

However, this equation only accounts for the mutual attraction of two objects in a circular orbit. Other factors that heavily affect a satellites trajectory are known as orbit perturbations. [2, 6]

### 3 Orbit Perturbations

Orbit perturbations, such as J2 perturbations, solar radiation, and atmospheric drag, all contribute to the trajectory of objects orbiting around the Earth. Due to these various factors, the motion of an object orbiting a non-perfect sphere will experience oscillations in its orbital trajectory.

#### 3.1 J2 Perturbations

Gravitational fields about a true spherical mass have an inverse relation. But because the Earth is not perfectly circular, a planets oblateness can affect the orbit of satellites. By having slightly flatter poles and a wider equator, a difference in forces causes a perturbation acceleration known as  $J_2$ . This aspherical nature of the Earth leads to a gravitational attraction that is no longer directed specifically towards the center of mass. The  $J_2$  perturbation is given by the following equation:

$$\ddot{\mathbf{r}} = \frac{3J_2\mu R_{Earth}^2}{2R^5} \left( \left(5 - \frac{r^2}{R^2} - 1\right) r_x + r_y \right) + r_z \left(5 - \frac{r^2}{R^2} - 3\right) \quad (11)$$

Here, the x, y, and z position vectors are represented in the Earth centered inertial frame (ECI). While the  $J_2$  perturbation is small, its effect significantly deviates the trajectory away from the pure inverse square motion. For a nearly circular orbit, the J2 perturbation acceleration equations can be added to the Clohessy-Wiltshire equations.

$$\ddot{\mathbf{x}} = \frac{3J_2 n^2 R^2}{2R_0} \left(1 - \frac{r_x}{R_0} (1 - 3\sin^2(nt)\sin^2(i)) + \frac{r_x}{R_0} (9\cos^2(nt) + 9\cos^2(i)\sin^2(nt) - 6) \right. \\ \left. + \frac{r_y}{R_0} (8\sin(nt)\cos(nt)\cos^2(i)) - \frac{r_z}{R_0} (8\sin(nt)\sin(i)\cos(i)) \right) \quad (12)$$

$$\ddot{\mathbf{y}} = \frac{3J_2 n^2 R^2}{2R_0} \left( \left(1 - \frac{7r_x}{R_0}\right) (\sin(2nt)\sin^2(i) + \frac{r_y}{R_0} (7\cos^2(nt) + 5\cos^2(i) - 4 - 7\cos^2(i)) - \frac{r_z}{R_0} (2\cos(nt)\sin(i)\cos(i)) \right) \quad (13)$$

$$\ddot{\mathbf{z}} = \frac{3J_2 n^2 R^2}{2R_0} \left( \left(1 - \frac{7r_x}{R_0}\right) \left( \frac{r_x}{R_0} (6\cos^2(i)\sin^2(i)\sin^2(nt)) \right) \right. \\ \left. + \frac{r_y}{R_0} (2\cos(nt)\sin(i)\cos(i)) - \frac{r_z}{R_0} (7\cos^2(i) + 5\cos^2(nt) - 4 - 5\cos^2(nt)\cos^2(i)) \right) \quad (14)$$

This can be simplified to a purely spherical harmonic expression:

$$\ddot{x} = \frac{\partial V}{\partial x} = \frac{\mu x}{r^3} \left(1 - J_2 \frac{3a_2 z^2}{r^2} (5 \frac{z^2}{r^2} - 1)\right) \quad (15)$$

$$\ddot{y} = \frac{\partial V}{\partial y} = \frac{\mu y}{r^3} \left(1 - J_2 \frac{3a_2 z^2}{r^2} (5 \frac{z^2}{r^2} - 1)\right) \quad (16)$$

$$\ddot{z} = \frac{\partial V}{\partial z} = \frac{\mu z}{r^3} \left(1 - J_2 \frac{3a_2 z^2}{r^2} (5 \frac{z^2}{r^2} - 1)\right) \quad (17)$$

While there are several orders of zonal harmonic perturbations, the second order is the most dominate. The second zonal harmonic for the Earth is known as the constant:

$$J_2 = 1.082629 \times 10^{-3}$$

Although other harmonics induce perturbations on orbiting objects, their contributions are overshadowed by the  $J_2$  perturbation as no other harmonics are greater an order of  $10^{-6}$ . As shown below, the effects of  $J_2$  perturbations on a 3.5 kg CubeSat oscillate steadily between 300 km and 288 km over a period of 4.5 days. However, once the altitude begins to rapidly drop, the oscillations become less severe. [2, 12, 5]

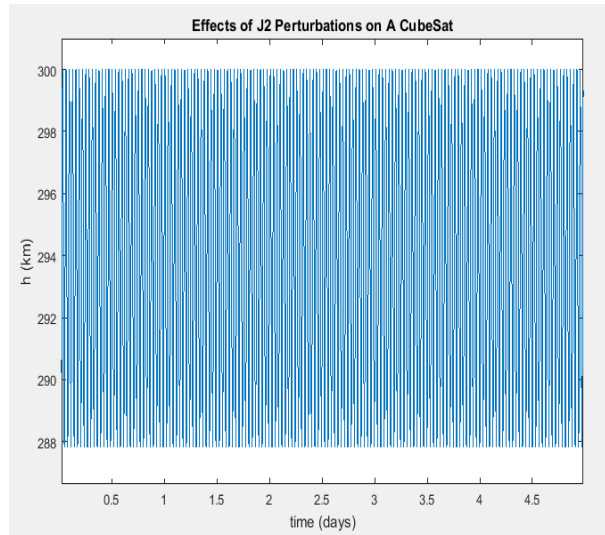


Figure 3: Influence of J2 perturbations for a 3.5 kg CubeSat with an orbit inclination of  $51.7^\circ$

### 3.2 Atmospheric Model

One of the driving factors in orbit perturbations stems from the relationship between density and altitude. The farther away a satellite travels from the Earth's atmosphere, the smaller the density becomes. While there are various methods for estimating Earth's atmospheric density model, one of the more accurate models is the Jacchia-Bowman 2008 (JB 2008). Originally developed as a revision to the 2006 model, JB 2008 builds upon Jacchia's diffusion equations by adding extreme solar irradiances, exospheric temperature equations, semiannual density equations based on multiple 81-day averaged solar indices, and geomagnetic storm effects. Determining variations in the ultraviolet solar radiation depend on two components: the solar rotational modulation of active region emission and the long-term evolution of the solar magnetic field. Jacchia utilized the following daily indices as key parameters for both his models:

- $F_{10}$ : The 10.7-cm solar radio flux is a flux density measurement of the total emission at a wavelength of 10.7 cm from all sources captured by the solar disk. The  $F_{10}$  has physical units of  $W m^{-2} Hz^{-1}$  but is often referred to in solar flux units (sfu). An 81-day centered average of  $F_{10}$  is expressed as  $\bar{F}_{10}$
- $S_{10}$ : The  $S_{10}$  variable is measured from the 26-34 nm solar EUV emission. It is then normalized and converted to sfu by means of linear regression using  $F_{10}$ . Most of the irradiances are dominated by the chromospheric He II line as well as other chromospheric and coronal lines, which comes from solar active regions. An 81-day centered average of the  $S_{10}$  can also be expressed as  $\bar{S}_{10}$ .
- $M_{10}$ : The  $M_{10}$  variable accounts for the chromospheric Mg II  $h$  and  $k$  lines as well as the photospheric wings. Its purpose is to measure the chromospheric and photospheric solar activity without the influence of instrument sensitivity. Once a linear regression with  $F_{10}$  has been achieved, the  $M_{10}$  is scaled to an index of sfu. An 81-day centered average of the  $M_{10}$  can also be expressed as  $\bar{M}_{10}$ .

- $Y_{10}$ : As photons arrive at Earth, they are primarily absorbed into the mesosphere and lower thermosphere by molecular oxygen and nitrogen to create the ionospheric D-region, also known as the  $X_{10}$  variable. While the 0.1-0.8 nm X-rays account for a major energy source during high solar activity in this atmospheric region, hydrogen (H) Lyman- $\alpha$  emissions dominate during moderate and low activity. Lyman- $\alpha$  emissions are formed in solar active regions when the photons are absorbed and dissociate nitric oxide (NO) and become involved in water ( $H_2O$ ) activity. In order to account for both solar emissions,  $Y_{10}$  was created as a mixed solar index to represent mostly  $X_{10}$  during solar maximum and Lyman- $\alpha$  during moderate and low solar activity. A normalized value of  $\bar{F}_{10}$  is used as the weighting function.

Until the creation of JB 2006, empirical atmospheric density models typically yielded errors between 15% - 20% due to the lack of modeling two important components: the semiannual density variation and an incomplete thermospheric heating parameter. The semiannual density variation was first discovered in 1961 through the analysis of satellite drag data. Scientists observed a 6-month periodicity maximum occurring in April and October and minimum's in January and July. Despite being a worldwide effect, the semiannual period was found to be only approximate as each max and min occurred at varying times from year to year. Jacchia found that the amplitude of the semiannual density variation was strongly dependent on altitude as shown in the following equation:

$$\Delta_{SA} \log_{10} \rho = F(z) G(t) \quad (18)$$

where  $G(t)$  represents the average density variation as a function of time and  $F(z)$  is the relation between the amplitude and height  $z$ . The average density variation consists of a Fourier series with nine coefficients representing a quad-annual variation over a 28-day smoothed density difference. Using the  $\bar{F}_{10}$ ,  $\bar{S}_{10}$ , and  $\bar{M}_{10}$  variables, a new solar index representing the long term EUV and FUV heating can be determined.

$$\bar{F}_{SM} = 1.00\bar{F}_{10} - .75\bar{S}_{10} - .37\bar{M}_{10} \quad (19)$$

Once the new solar index is calculated, the yearly semiannual phase variations can be used to model the average density variation.

$$G(t) = C_1 + C_2 \sin(\omega) + C_3 \cos(\omega) + C_4 \sin(2\omega) + C_5 \cos(2\omega) + \bar{F}_{SM} (C_6 + C_7 \sin(\omega) + C_8 \cos(\omega) + C_9 \sin(2\omega) + C_{10} \cos(2\omega)) \quad (20)$$

where coefficient values with standard deviations are determined from best fit results obtained from satellite data.

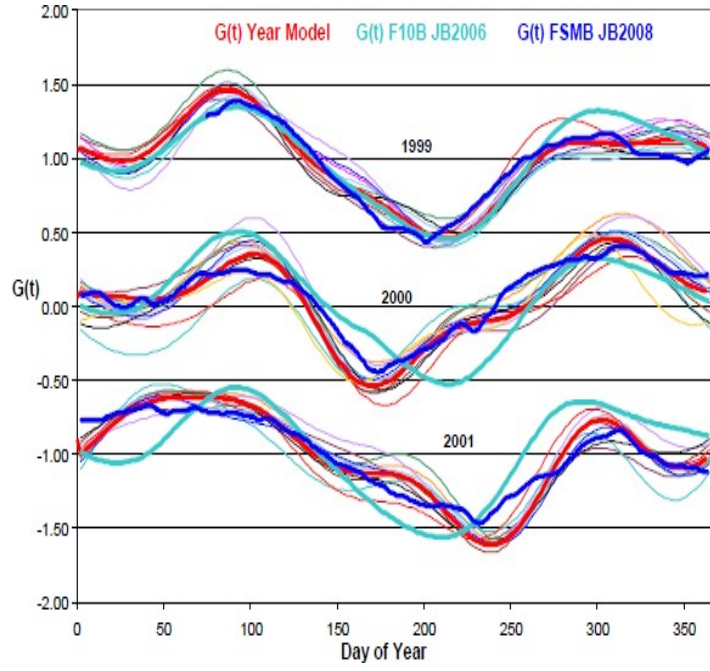


Figure 4: Average density variation as a function of time and  $F(z)$  for three different years [1]

The semiannual height function,  $F(z)$ , was determined on a yearly and satellite-by-satellite basis by a nine term Fourier series. The  $F(z)$  value was then computed for each fit as the difference of minimum and maximum values for that given year. Similar to the  $G(t)$  function, a new solar index representing the semiannual variation can be calculated using the  $\bar{F}_{10}$ ,  $\bar{S}_{10}$ , and  $\bar{M}_{10}$  variables.

$$\bar{F}_{SM} = 1.00\bar{F}_{10} - 0.70\bar{S}_{10} - 0.04\bar{M}_{10} \quad (21)$$

The  $\bar{F}_{SM}$  is then used to determine the new height index as follows:

$$F(z) = B_1 + B_2\bar{F}_{SM} + B_3z\bar{F}_{SM} + B_4z^2\bar{F}_{SM} + B_5z\bar{F}_{10}^2 \quad (22)$$

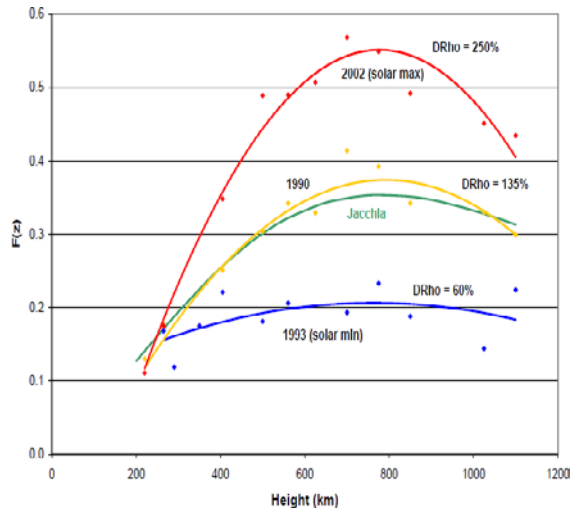


Figure 5: Amplitude function  $F(z)$  for three different years with semiannual amplitudes plotted vs height[1]

Modeling geomagnetic storms form an important part of correctly calculating atmospheric density. Geomagnetic storm modeling is monitored through the Disturbance Storm Time (Dst) index and is primarily used to determine the strength of the storm within the inner magnetosphere. During the primary phase of the storm, the storm-time ring becomes highly energized and generates a southward-directed magnetic field perturbations at lower altitudes. When compared with data from satellites, the JB 2008 model is extremely consistent with orbit altitudes of 400 and 500 km. [1]

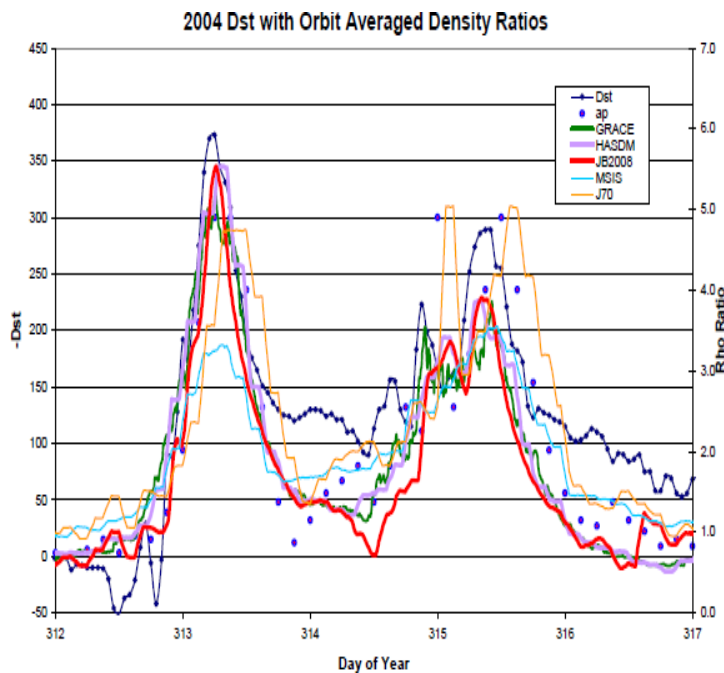


Figure 6: Major 2004 storms with Dst and density ratios displayed [1]

The relationship between density and altitude for a specific day and latitude/longitude pair can be expressed by an exponential correlation. While an exponential density model provides

a simple relationship between density and altitude, the accuracy decreases the closer it gets to the Karmin line. As shown in the following figure, the JB 2008 model provides a much lower density distribution for a given longitude and latitude.

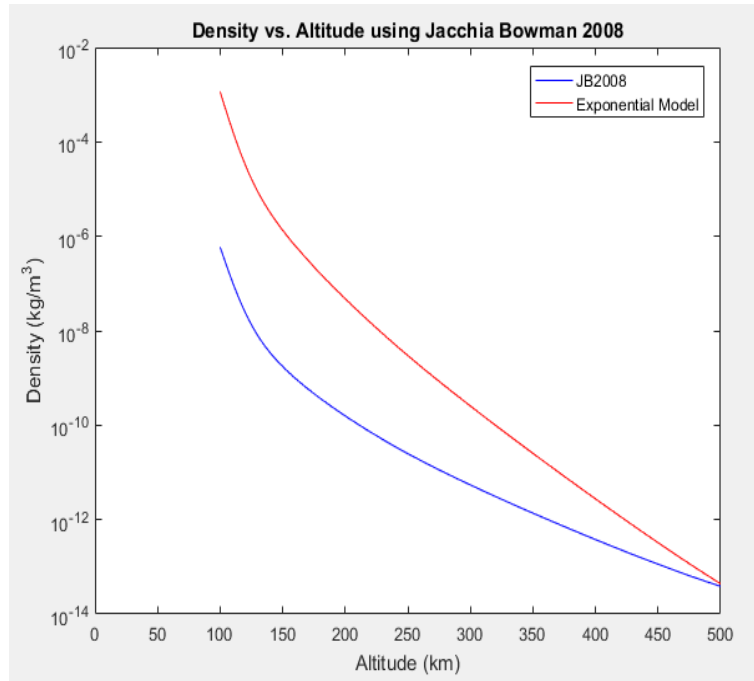


Figure 7: JB 2008 altitude plot versus exponential density estimation

Another atmospheric model commonly used to reproduce temperature and density from ground to space is NRLMSISE-00, an empirical, global model of Earth's atmosphere based on actual satellite drag data. Developed by the US Naval Research Laboratory (NRL), MSIS, or mass spectrometer and incoherent scatter radar, has become the standard for international space research in predicting satellite decay due to atmospheric drag. However, MSIS accuracy often suffers both before and after storm periods as a result of not correctly modeling the solar EUV data. The following figure shows the comparison of MSIS and JB 2008 on a given day as a function of altitude. Both models portray accurate density readings at lower altitudes, but tend to differ farther away from the Karman altitude due to the increasing effect of solar events.

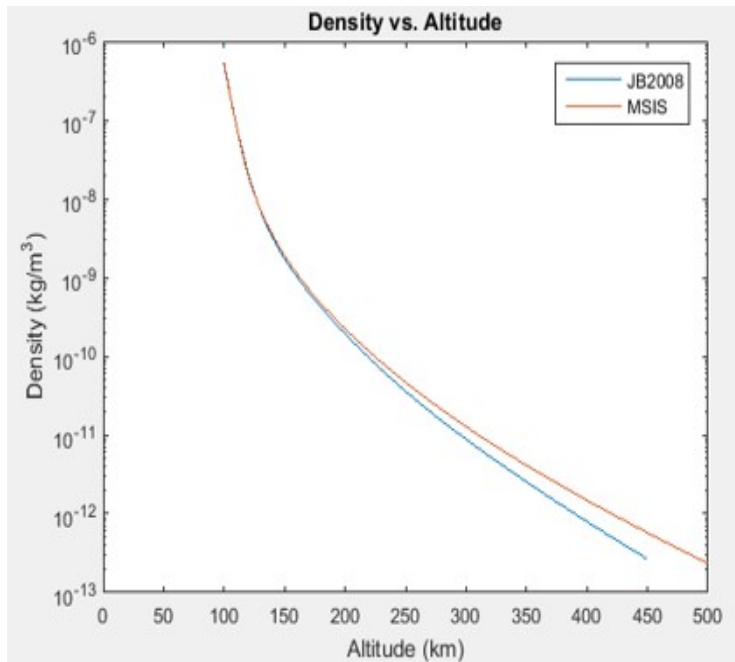


Figure 8: JB 2008 altitude plot versus MSIS on April 10, 2017

After inputting the Earth orientation parameters, space weather data, and geomagnetic storm values, the density can be calculated as functions of altitude, longitude, and latitude for any given day. The following plots show the density variation across the globe at 300 km for different seasons of the year.

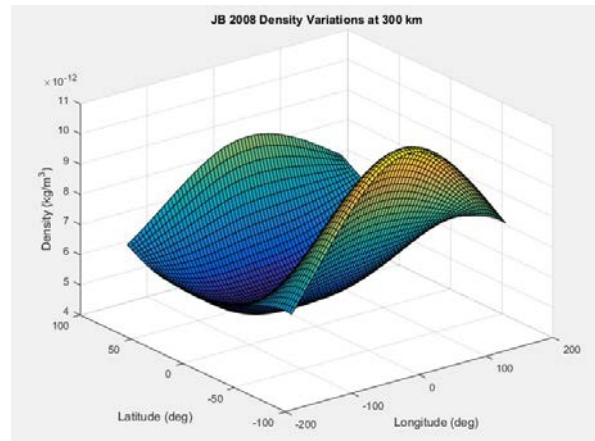
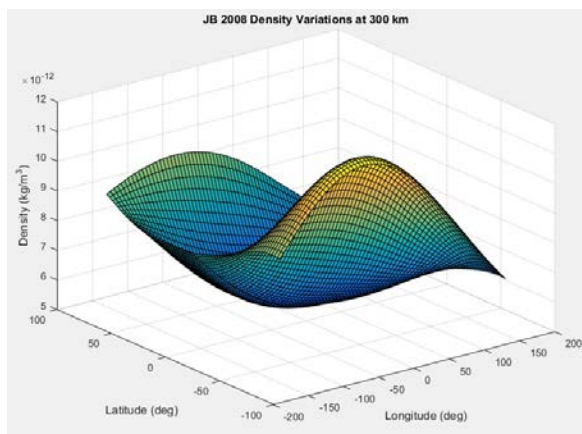


Figure 9: Density distribution as a function of longitude and altitude at 300 km for the winter and spring of 2016 respectively

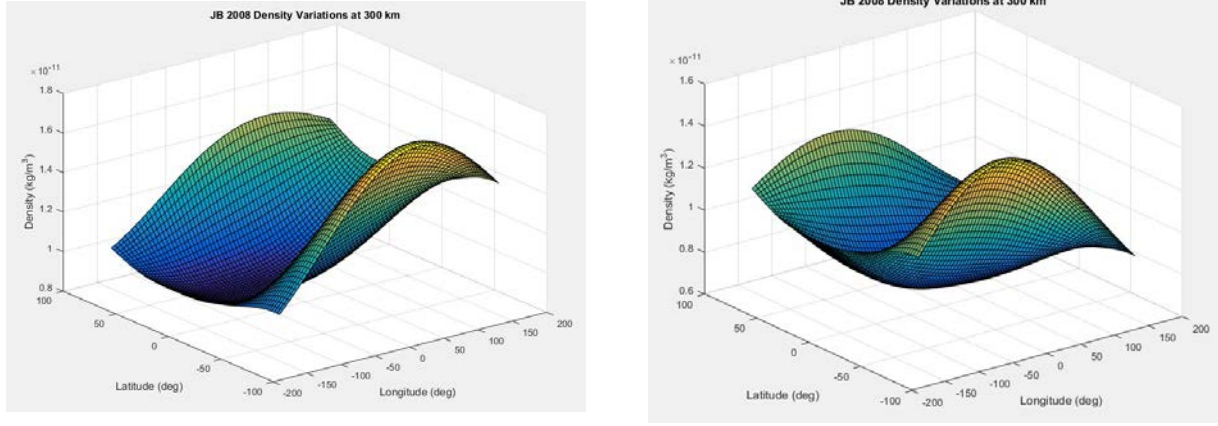


Figure 10: Density distribution as a function of longitude and altitude at 300 km for the summer and fall of 2016 respectively

As shown, the density is greatest in the spring, causing the orbital lifetime to decrease when compared to the other seasons. Results from the Canadian Center of Science and Education indicate that there is a higher probability of producing an intense geomagnetic storm at the equinoxes than at the solstices, heating up and expanding the Earth's upper atmosphere. As the heat rises, the density above the Karman line increases significantly, thus creating more drag and decreasing the mission time of the satellite when these storms occur. While geomagnetic storms can occur in any month, the greater density of storms are produced around the solar maximum solar cycle and during the descending phase of the solar cycle. In addition to having a correlation to the season, density is also affected by its location around the globe. Due to various effects like geomagnetic storms and increased solar ultraviolet emission, Earth's upper atmosphere around the lower to mid latitudes tend to be more dense than either of the poles, producing increased drag in these locations [8].

### 3.3 Atmospheric Drag

Atmospheric drag affects all satellites orbiting the Earth and is the most significant source of error in modeling their trajectory. At any orbital altitude, atmospheric drag occurs when gas molecules frequently collide with the satellite and accounts for the primary cause for orbital decay in low Earth orbit (LEO). This momentum transfer between the molecules in the atmosphere and the spacecraft form the underlying cause of atmospheric drag. Like a positive feedback effect, a lower altitude corresponds with a faster orbital decay rate due to an increase in atmospheric density, aerodynamic drag, and heating. Determining the atmospheric drag force becomes one of the most important parameters when propagating a satellite's trajectory. The most widely accepted equation for atmospheric drag is as follows:

$$\mathbf{a}_{drag} = -\frac{1}{2} C_D \left( \frac{A}{M} \right) \rho V^2 \frac{\mathbf{v}_{rel}}{|\mathbf{v}_{rel}|} \quad (23)$$

$$\text{where, } \mathbf{v}_{rel} = \mathbf{v}_{sat} + \mathbf{v}_{atmo} \quad (24)$$

Here,  $C_D$  is the drag coefficient,  $A$  is the reference area,  $m$  is the mass,  $\rho$  is the atmospheric density, and  $\mathbf{v}_{rel}$  is the velocity relative to the spacecraft. Aerodynamic forces and moments are the reaction of an object doing work on the medium it is traveling in. The momentum and energy exchanged between the object and the medium depends on various factors such as mass distribution of the medium, geometry of the object, and characteristics of the objects surface. The duration of the interaction between the spacecraft and atmosphere plays an important role. There must be enough time for collisions among gas particles to equilibrate as well as fluid particles to redistribute energy and momentum. The common approximation for the drag coefficient is as follows:

$$C_D = \frac{2m\mathbf{a}_{drag}|\mathbf{v}_{rel}|}{\rho v_{rel}^2 A \mathbf{v}_{rel}} \quad (25)$$

This approximation is only appropriate when the mean free path between collisions among gas particles is much greater than the length scale of the problem or when the interaction time between the spacecraft and fluid is much higher than the time between particle collisions.

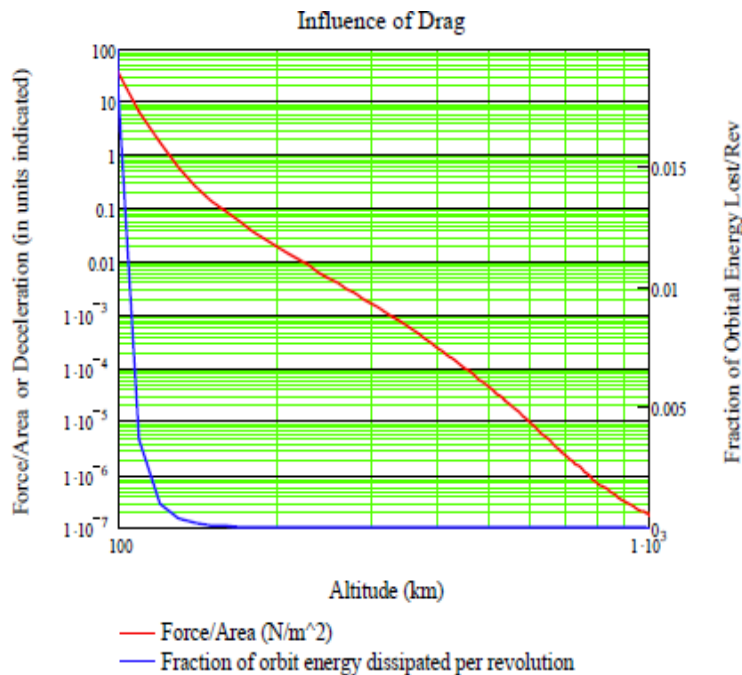


Figure 11: Influence of Drag for a 1000 kg satellite with a 100  $m^2$  drag area and a  $C_D = 2.2$  using a Harris-Preister atmospheric model [14]

The difficulty in determining the atmospheric drag force is that none of the above variables are exactly known. For example, the drag coefficient, while unique for each satellite, depends on the type of scattering between the surface of the structure and the neutral particles in the atmosphere. Because there are fundamental unknowns in the physics of scattering, it is impossible to reliably predict how particles in free motion behave under that specific condition. As shown in the previous section, the density can greatly vary depending on the time of year, the solar radiation from the sun of that specific day, geomagnetic storms, or position around the Earth, depending on which atmospheric model is chosen. However, an increase in density will

lead to an increase in drag acceleration, effectively speeding up the orbital decay rate. Using the Jacchia Bowman 2008 atmospheric model, the influence of atmospheric drag on a CubeSat with a drag device can be shown as follows. [4, 15, 6, 14, 2]

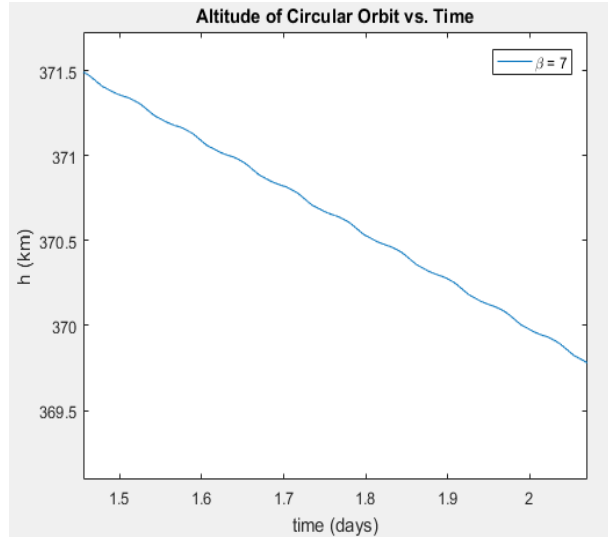


Figure 12: Influence of Drag for a 3.5 kg CubeSat with a  $0.2027 \text{ m}^2$  drag area and a  $C_D = 2.2$  using a JB 2008 atmospheric model

### 3.4 Gauss Variational Equations

When a perturbing acceleration acts on a system in orbit, the orbital elements will experience oscillations over time and drift away from their initial values. If a perturbing acceleration expressed in the inertial XYZ frame is

$$\mathbf{p} = p_x \mathbf{i} + p_y \mathbf{j} + p_z \mathbf{k} \quad (26)$$

and expressed in the non-inertial rsw frame as

$$\mathbf{p} = p_x \mathbf{r} + p_y \mathbf{s} + p_z \mathbf{w} \quad (27)$$

then the transformation between these two frames can be written as

$$\begin{bmatrix} p_r \\ p_s \\ p_w \end{bmatrix} = [Q]_{Xr} \begin{bmatrix} p_x \\ p_y \\ p_z \end{bmatrix} \quad (28)$$

Here, each row of  $[Q]_{Xr}$  is the direction cosines of the unit vectors for  $\mathbf{r}$ ,  $\mathbf{s}$ , and  $\mathbf{w}$  to relative the XYZ axes:

$$\begin{bmatrix} -\sin \Omega \cos i \sin u + \cos \Omega \cos u & \cos \Omega \cos i \sin u + \sin \Omega \cos u & \sin i \sin u \\ -\sin \Omega \cos i \sin u - \cos \Omega \sin u & \cos \Omega \cos i \cos u + \sin \Omega \cos u & \sin i \sin u \\ \sin \Omega \sin i & -\cos \Omega \sin i & \cos i \end{bmatrix} \quad (29)$$

where  $\Omega$  is the right ascension of the ascending node,  $i$  is the inclination, and  $u$  is the oscillating element. The transformation from XYZ to rsw is a rotation about the normal  $\mathbf{w}$

through the true anomaly,  $\theta$ . With this mapping, the time deviates for the oscillating orbital elements  $h, e, \theta, \Omega, i, \text{ and } \omega$  can be derived to form the Gauss planetary equations when looking at the perturbations due to  $J_2$ . As stated earlier, the time derivative of angular momentum is the cross product between the position and velocity vectors. Using the definition of the magnitude of a vector, the time rate of change for angular momentum can be expressed as

$$\frac{dh}{dt} = \frac{d}{dt} \sqrt{\mathbf{h} \cdot \mathbf{h}} = \frac{1}{2} \frac{1}{\sqrt{\mathbf{h} \cdot \mathbf{h}}} \left( 2\mathbf{h} \cdot \frac{d\mathbf{h}}{dt} \right) = \frac{\mathbf{h}}{h} \cdot \frac{d\mathbf{h}}{dt} = \mathbf{w} \cdot \frac{d\mathbf{h}}{dt} \quad (30)$$

Substituting the cross product for the time rate of change of the angular momentum vector and utilizing the vector identity,

$$\frac{d\mathbf{h}}{dt} = (\mathbf{w} \times \mathbf{r}) \cdot \mathbf{p} \quad (31)$$

From the relationships derived earlier, the cross product between  $\mathbf{w}$  and  $\mathbf{r}$  will be in the  $\mathbf{s}$  direction and  $\mathbf{r} = r\hat{\mathbf{r}}$ , the expression can be simplified to

$$\frac{dh}{dt} = rp_s = r\mathbf{p} \cdot \mathbf{s} \quad (32)$$

It becomes clear that the variation of angular momentum depends solely on the transverse perturbation components, meaning that only the local horizon component of a perturbing acceleration will change the angular momentum over time.

The change in eccentricity over time can be derived from differentiating the scalar form of  $e$ ,

$$e = \frac{h^2}{\mu^2} \left( \frac{1}{r} - \frac{2\mu}{v^2} \right) \quad (33)$$

with the velocity vector and the relations  $\partial v^2 / \partial \mathbf{v} = 2\mathbf{v}$  and  $\partial h^2 / \partial \mathbf{v} = 2\mathbf{h} \times \mathbf{r}$ , the change in eccentricity over time equates to

$$\frac{\partial e}{\partial \mathbf{v}} = \frac{1}{\mu^2 e} \left( h^2 \mathbf{v} \cdot \mathbf{r} + h\mathbf{r} \cdot \left( v^2 - \frac{2\mu}{r} \right) + h^2 \mathbf{v} \cdot \mathbf{s} \right) \quad (34)$$

Knowing that  $\mathbf{v}_s$  is the same as  $\mathbf{v}_\perp$ , and rearranging the orbit equation, the new expression becomes

$$\frac{\partial e}{\partial \mathbf{v}} = \frac{h}{\mu} \sin \theta \mathbf{r} + \frac{1}{\mu h} (h^2 + \mu r) \cos \theta + \mu e \mathbf{s} \quad (35)$$

After substituting for  $\mathbf{r}$  and  $\mathbf{p}$ , the final form can be shown as

$$\frac{de}{d\mathbf{v}} = \frac{h}{\mu} \sin \theta \mathbf{p}_r + \frac{1}{\mu h} (h^2 + \mu r) \cos \theta + \mu e \mathbf{p}_s \quad (36)$$

Unlike the angular momentum, the eccentricity is affected by perturbations that lie only in the orbit plane.

Variation of the true anomaly can be first expressed as

$$\frac{d\theta}{dt} = \frac{h}{r^2} + \frac{\partial\theta}{\partial\mathbf{v}} \cdot \mathbf{p} \quad (37)$$

To solve for the partial derivative expression, the orbit equation combined with the radial speed formula can be rearranged to obtain

$$[(h^2 - \mu r)\cos\theta + h(\mathbf{r} \cdot \mathbf{v})\sin\theta] \frac{\partial\theta}{\partial\mathbf{v}} = h \frac{\partial(\mathbf{r} \cdot \mathbf{v})}{\partial\mathbf{v}} \cos\theta + [(\mathbf{r} \cdot \mathbf{v})\cos\theta - 2h\sin\theta] \frac{\partial h}{\partial\mathbf{v}} \quad (38)$$

Simplifying the above equation and utilizing  $\partial(\mathbf{r} \cdot \mathbf{v})/\partial\mathbf{v}$  and  $\partial h/\partial\mathbf{v} = (\mathbf{h} \times \mathbf{r})/h$  leaves

$$\frac{\partial\theta}{\partial\mathbf{v}} = \frac{h}{\mu e} \cos\theta \mathbf{r} - \frac{1}{e} \left( \frac{h^2}{\mu} + r \right) \frac{\sin\theta}{h} \mathbf{s} \quad (39)$$

Recalling that  $\mathbf{s} = \mathbf{w} \times \mathbf{r}$  and substituting the above equation into the original equation yields the time variation of true anomaly due to a perturbing acceleration. Like eccentricity, true anomaly is only affected by perturbations within the orbit plane.

$$\frac{d\theta}{dt} = \frac{h}{r^2} + \frac{1}{eh} \frac{h^2}{\mu} \cos\theta p_r - \left( \frac{h^2}{\mu} + r \right) \sin\theta p_s \quad (40)$$

The right ascension of the ascending node can be found as the angle between the nodal line,  $\mathbf{N}$ , and the z-component in the inertial frame.

$$\cos\Omega = \sqrt{\frac{\mathbf{N} \cdot \hat{\mathbf{i}}}{\mathbf{N} \cdot \mathbf{N}}} \quad (41)$$

It can also be represented in terms of the angular momentum vector and its components as

$$\tan\Omega = \frac{\mathbf{h} \cdot \hat{\mathbf{i}}}{\mathbf{h} \cdot \hat{\mathbf{j}}} \quad (42)$$

Taking the time derivative of the above equation and simplifying some algebra leaves

$$\frac{d\Omega}{dt} = \cos^2\Omega \frac{d\mathbf{h}}{dt} \cdot \frac{h_x \hat{\mathbf{j}} - h_y \hat{\mathbf{i}}}{h} \quad (43)$$

Because the angular momentum vector is in the same direction as  $\mathbf{w}$ , utilizing the transformation of  $\mathbf{w}$  to the  $XYZ$  coordinate system leaves

$$\frac{d\Omega}{dt} = \frac{d\mathbf{h}}{dt} \cdot \frac{h \sin i (\cos\Omega \hat{\mathbf{i}} + \sin\Omega \hat{\mathbf{j}})}{(h \sin i)^2} = \frac{1}{h \sin i} \hat{\mathbf{N}} \cdot \frac{d\mathbf{h}}{dt} \quad (44)$$

where  $\hat{\mathbf{N}}$  is the unit vector along the line of nodes. Substituting the cross product of  $\mathbf{r}$  and  $\mathbf{p}$  for the time derivative of  $\mathbf{h}$  and utilizing the vector identity between a cross and dot product, the equation simplifies to

$$\frac{d\Omega}{dt} = \frac{r \sin u}{h \sin i} \mathbf{w} \cdot \mathbf{p} = \frac{r \sin u}{h \sin i} p_w \quad (45)$$

An orbits inclination can be expressed as the angle between the angular momentum vector

and the  $z$ -axis of the inertial reference frame

$$\cos i = \frac{\mathbf{h} \cdot \mathbf{k}}{h} \quad (46)$$

Differentiating with time and using the definition of a dot product yields

$$\frac{di}{dt} \sin i = \frac{r}{h} (\mathbf{w} \cos i - \mathbf{k}) \cdot (\mathbf{r} \times \mathbf{p}) \quad (47)$$

Inserting the transformation of  $\mathbf{w}$  to the  $XYZ$  coordinate system and interchanging the dot and cross products leaves

$$\frac{di}{dt} = \frac{r}{h} \sin \Omega \cos \mathbf{i} - \cos \Omega \cos \mathbf{j} - \sin \mathbf{k} \times \mathbf{r} \cdot \mathbf{p} \quad (48)$$

After taking the cross and dot products, the time variation of inclination simplifies to

$$\frac{di}{dt} = \frac{r}{h} \cos u \frac{p}{w} \quad (49)$$

Looking at the relationship between the argument of periapsis and latitude,

$$\omega = u - \theta \quad (50)$$

the variation of argument of periapsis can be expressed as

$$\frac{d\omega}{dt} = \frac{du}{dt} - d\theta/dt \quad (51)$$

Because the variation of true anomaly was solved earlier, computing the expression for  $d\omega/dt$  relies on first solving for  $du/dt$ . Upon rearranging the radial unit vector  $\mathbf{r}$  from the transformation matrix found previously, the time rate of change for  $\mathbf{u}$  can be expressed as

$$\frac{\partial \mathbf{u}}{\partial t} = -\cos i \frac{\partial \Omega}{\partial \mathbf{r}} \quad (52)$$

Substituting for  $\partial \Omega / \partial t$  and dotting with  $\mathbf{p}$ , the expression can be simplified to

$$\frac{\partial \mathbf{u}}{\partial \mathbf{r}} = -\frac{r \sin u}{h \tan i} \mathbf{w} \quad (53)$$

Inputting the results into the original equation and substituting the variation of true anomaly, the variation of argument of periapsis can be expressed as

$$\frac{d\omega}{dt} = -\frac{1}{eh} \frac{h^2}{\mu} \cos \theta p_r - \left( r + \frac{h^2}{\mu} \right) \sin \theta p_s - \frac{r \sin(\omega + \theta)}{h \tan i} p_w \quad (54)$$

Unlike the other orbital elements, the argument of periapsis is affected by all three components of the perturbing acceleration. This analysis allows for the observation of different perturbing forces and their effects on an orbit's geometry. Whether a  $J_2$  perturbation, atmospheric drag, or a tangential thrust, the perturbing acceleration variable can be modified to simulate each case and show how orbital elements will drift over time due to outside forces. When looking at the effects of  $J_2$  gravitational perturbations in particular, the perturbation

accelerations  $p_r$ ,  $p_s$ , and  $p_w$  in the Gauss variation equations can be substituted to form the Gauss planetary equations.

$$\frac{dh}{dt} = -\frac{3 J_2 \mu R^2}{2 r^3} \sin^2 i \sin 2u \quad (55)$$

$$\frac{de}{dt} = \frac{3 J_2 \mu R^2}{2 h r^3} \frac{h^2}{\mu r} \sin \theta (3 \sin^2 i \sin^2 u - 1) - \sin 2u \sin^2 i [(2 + e \cos \theta) \cos \theta + e] \quad (56)$$

$$\frac{d\theta}{dt} = \frac{h}{r^2} + \frac{3 J_2 \mu R^2}{2 h r^3} \frac{h^2}{\mu r} \cos \theta (3 \sin^2 i \sin^2 u - 1) + (2 + e \cos \theta) \sin 2u \sin^2 i \sin \theta \quad (57)$$

$$\frac{d\Omega}{dt} = -\frac{3 J_2 \mu R^2}{2 h r^3} \sin^2 i \cos i \quad (58)$$

$$\frac{di}{dt} = -\frac{3 J_2 \mu R^2}{4 h r^3} \sin 2u \sin 2i \quad (59)$$

$$\frac{d\omega}{dt} = \frac{3 J_2 \mu R^2}{2 e h r^3} \frac{h^2}{\mu r} \cos \theta (1 - 3 \sin^2 i \sin^2 u) - (2 + e \cos \theta) \sin 2u \sin^2 i \sin \theta + 2 e \cos^2 i \sin^2 u \quad (60)$$

When looking at a satellite orbiting around earth with a radius of perigee of 6678 km, radius of apogee of 9440 km, an inclination of 28 °,  $\Omega$  of 45 °, and a  $\omega$  of 30 °, the variation of orbital elements due to  $J_2$  perturbations looks as shown in the following figure. While the inclination and eccentricity oscillate slightly, the argument of perigee and right ascension have a somewhat linear relationship as time increases. Based off these six orbital elements, other elements such as semimajor axis, eccentric anomaly, and mean anomaly can all be calculated from these variation equations.

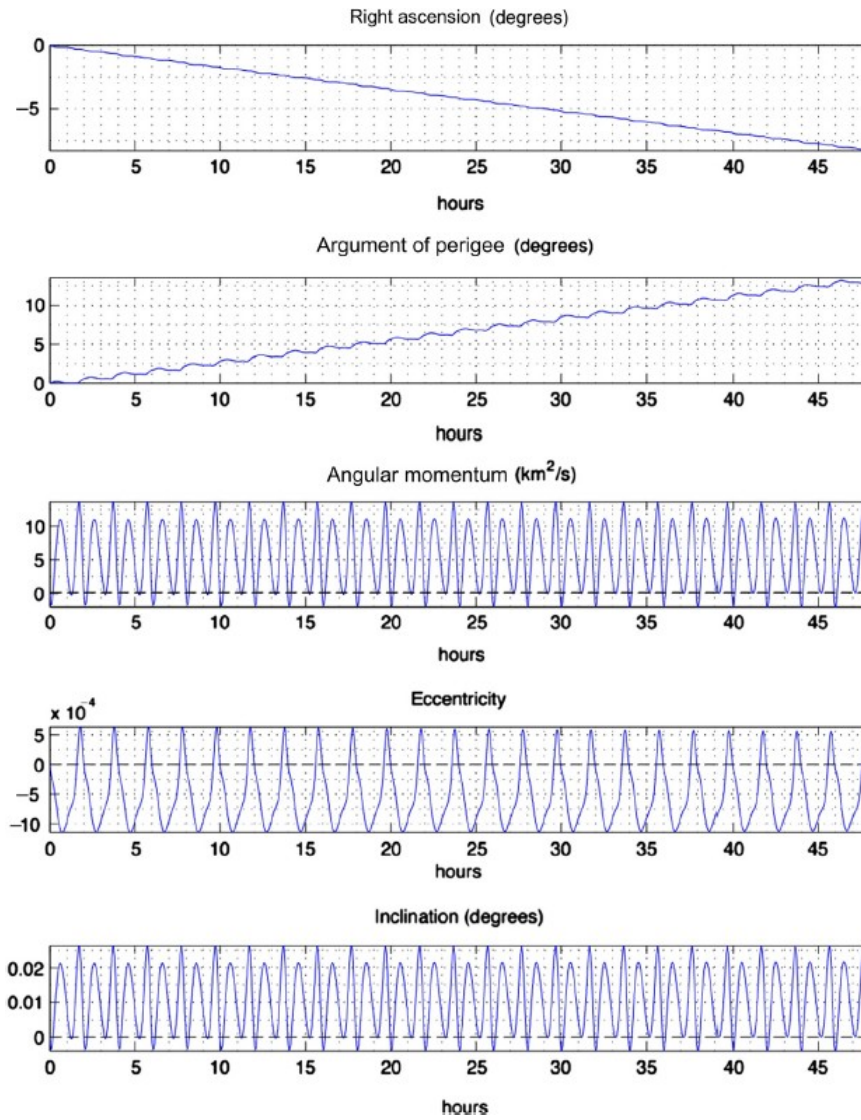


Figure 13: Variation of orbital elements due to  $J_2$  perturbations over time [2]

## 4 De-Orbit Maneuver

Without thrusters to keep the spacecraft in orbit, CubeSats jettisoned from their deployers follow a de-orbit trajectory. A de-orbit, or re-entry trajectory, is usually a slow orbit decay from which the spacecraft will continue to lose altitude over time and eventually re-enter into the atmosphere. Factors such as atmospheric conditions, ballistic coefficient, and propulsive devices all contribute to the duration of the de-orbit. While the majority of cubesats will disintegrate during re-entry, some components containing heavy metals or heat tolerant materials will not vaporize in this time period. Larger satellites perform precise burn to safely guide the remaining debris away from people on the ground. However, a spacecraft with no propulsive device offers no ability to target a location, posing as a potential danger. Because propulsive devices are somewhat difficult to integrate with the limited storage capacity of CubeSats, it becomes a challenge to steer hazardous debris away from the mainland. One option becoming increasingly attractive is drag modulation. [11, 3, 10]

## 4.1 Drag Modulation

Drag modulation aims at varying the drag of a spacecraft in order to increase or decrease the duration of the mission. This can be done by changing the surface area exposed to the atmospheric drag, thus increasing or decreasing its air resistance. The ballistic coefficient, or a measure of an objects ability to overcome air resistance, can be used as a benchmark for modulating the drag.

$$\beta = \frac{m}{c_D A} \quad (61)$$

The ballistic coefficient is inversely proportional to the negative acceleration, meaning that a high number represents a lower drag on the body. Increasing the effective surface area will then decrease the ballistic coefficient, effectively decreasing the duration of the mission. TechEdSat’s solution to drag modulation is with an Exo-Brake. Similar to a parachute, the Exo-Brake is a drag device capable of changing surface area through a single winch design. By retracting the winch, two of the sides pull in to decrease the surface area and increase the ballistic coefficient. As shown in the following figure, precise winch control allows for various surface area configurations.

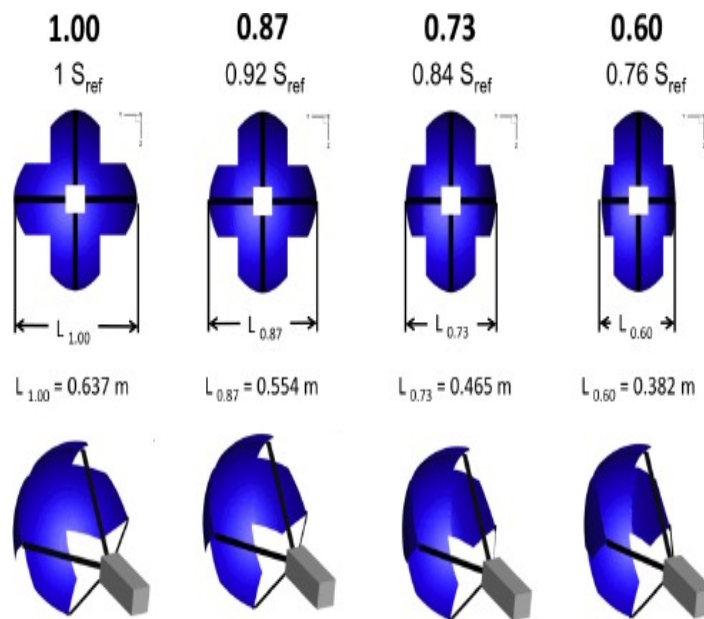


Figure 14: Potential Exo-Brake configurations through a winch system [3]

Using the Program to Optimize Simulated Trajectories II (POST2), a team at NASA Langley was able to simulate TechEdSat 4’s end-to-end, or ISS to Earth surface, trajectory using various Exo-Brake deployment configurations. POST2 is a 6-degree-of-freedom, generalized point mass, rigid body, discrete parameter targeting and trajectory optimization simulator capable of simulating up to 20 independent or connected rigid bodies. However, for their analysis,

the attitude was constrained to an angle of attack and sideslip angles of  $0^\circ$ , essentially modeling the satellite as a 3-degree-of-freedom vehicle. By limiting the movement, the only aerodynamic force acting on the body can be assumed to be the axial force.

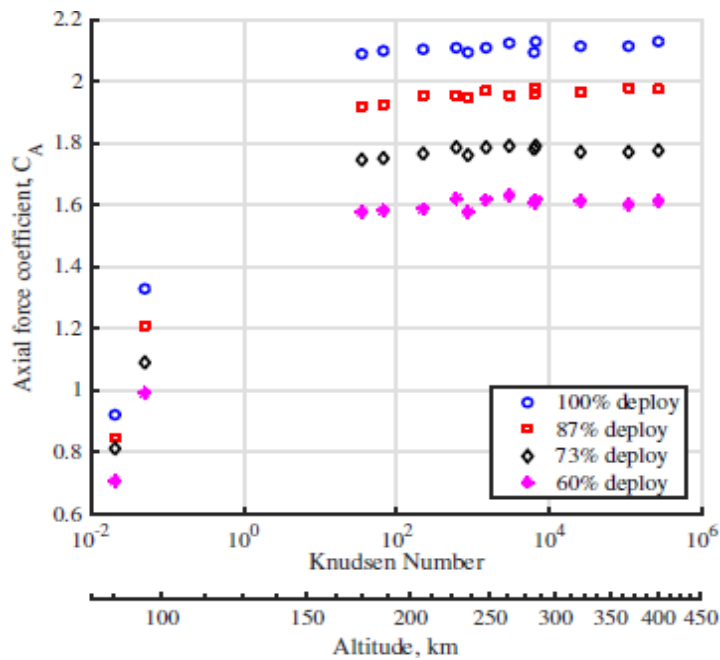


Figure 15: Potential Exo-Brake configurations through winch system [3]

As expected, the highest axial force is generated when the Exo-Brake is fully deployed and is lowest at 60% (0.76 of maximum surface area) deployed, the maximum retractable state of the drag device. At higher altitudes, the axial forces become relatively constant due to the exponential decay of density values.

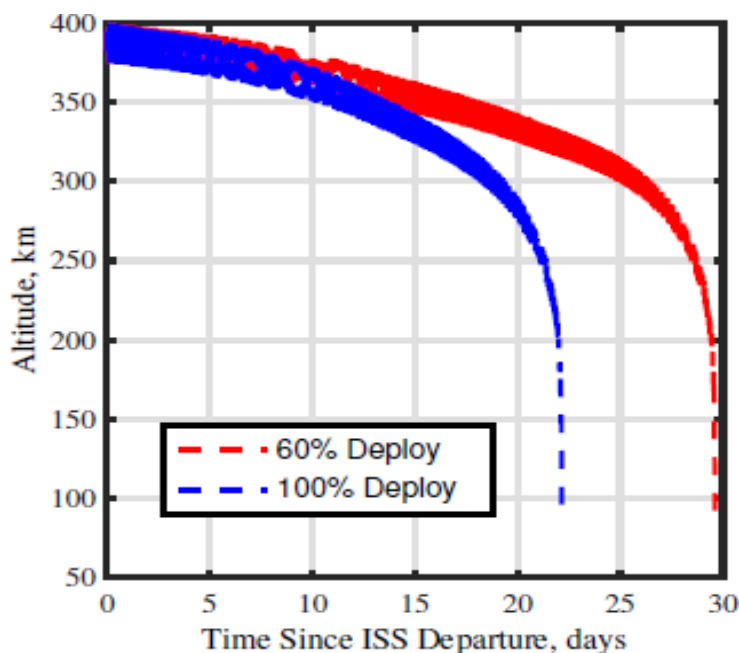


Figure 16: Days since ISS departure for both 60% and 100% deployments [3]

In addition to targeting re-entry positions, drag modulation can be used to speed up the duration of the mission. As shown in the figure above, the Exo-Brake can alter the time until re-entry by 7-8 days depending on the deployment configuration and atmospheric conditions. This indicates that modulating the drag can provide a reasonable window of time for a guidance scheme without the use of a propulsion device, given that a typical orbit of previous TechEdSat's were around 90 minutes.

The research team at NASA Langley used a predictor-corrector type of algorithm for an end-to-end trajectory in the POST2 software to simulate Exo-Brake de-orbit targeting. This algorithm is based on the cost function of the run, a projected-gradient based optimizer that modifies the deployment time and level until the optimum trajectory is achieved. A basic predictor-corrector algorithm is designated to integrate ordinary differential equations to find an unknown function that satisfies a given differential equation. Each algorithm can be devised into two main steps:

1. The initial, "prediction" step begins from a function fitted to the function-values and derivative-values with initial conditions and extrapolates, or anticipates, the said function at subsequent points.
2. The next, "corrector" step refines the initial approximation from the predicted value of the function with an additional method to interpolate the unknown functions' value at identical subsequent points.

While the exact algorithm used in the POST2 software was not provided, the following figure shows the result of a 1200 case Monte Carlo simulation with minimum drag modulations aiming for a 50 km circle around the target. As shown, 87% of the cases landed within the desired range with only 7 total drag deployment sequences. However, increased accuracy can be achieved by allowing more modulations at the cost of an increased chance for failure.[3]



Figure 17: Landing points from a Monte Carlo simulation [3]

## 4.2 Gravity Gradient and Aerodynamic Torque

At higher altitudes, the atmospheric torque generated by the Exo-Brake will be insufficient to overcome the torque due to the gravity gradient. The gravity gradient torque results when portions of a non-symmetric satellite are subjected to a slightly larger forces the closer it is to the central body. This force imbalance creates a tendency for the satellite to orient with its long axis pointing towards the center of the central body. The worst case gravity gradient torque can be modeled as follows:

$$T_g = \frac{3\mu}{2R^3} |I_z - I_y| \cos(2\theta), \quad (62)$$

where  $I_z$  and  $I_y$  represent the maximum and minimum moments of inertia,  $R$  is the radius from the center of the Earth to the center of gravity of the spacecraft, and  $\theta$  is the maximum deviation of the z-axis from the local vertical with a worst case scenario of  $45^\circ$ . The gravity gradient torque acting on T5 (3U) and T7 (2U) varies with altitude as shown:

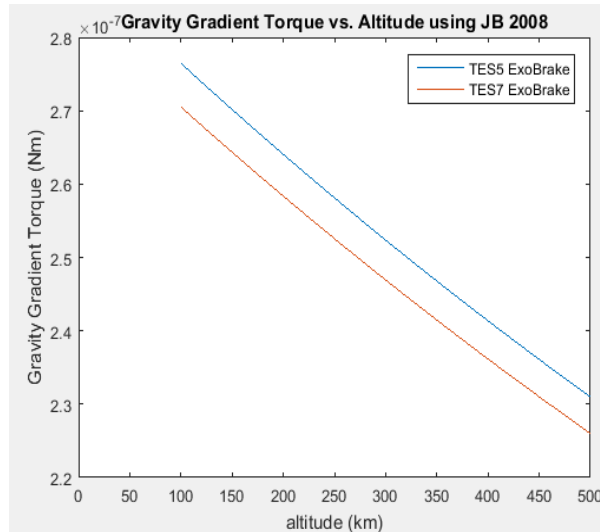


Figure 18: Gravity gradient torque acting on T5 and T7 [9]

In order for the drag device to provide any stability or control capabilities, the aerodynamic torque must be able to overcome the gravity gradient torque. The aerodynamic drag force can be universally defined as:

$$F_{drag} = \frac{1}{2} \rho C_D A V^2 \quad (63)$$

The torque can then be defined as the the aerodynamic forces times the lever arm, which is the distance between the satellites center of mass and the centroid of the drag force. Five scenarios were tested to simulate various Exo-Brake configurations and orientations at  $-90^\circ$  angle of attack: a normal inflated "flat-top", vane strip surface area, full hemisphere, T5 surface area, and a normal T7 respectively. An AoA of  $-90^\circ$  was chosen as the worst case orientation for controllability due to the smallest possible reference surface area collecting drag. The corresponding drag forces and aerodynamic torques were computed as a function of altitude using the JB 2008 atmospheric model.

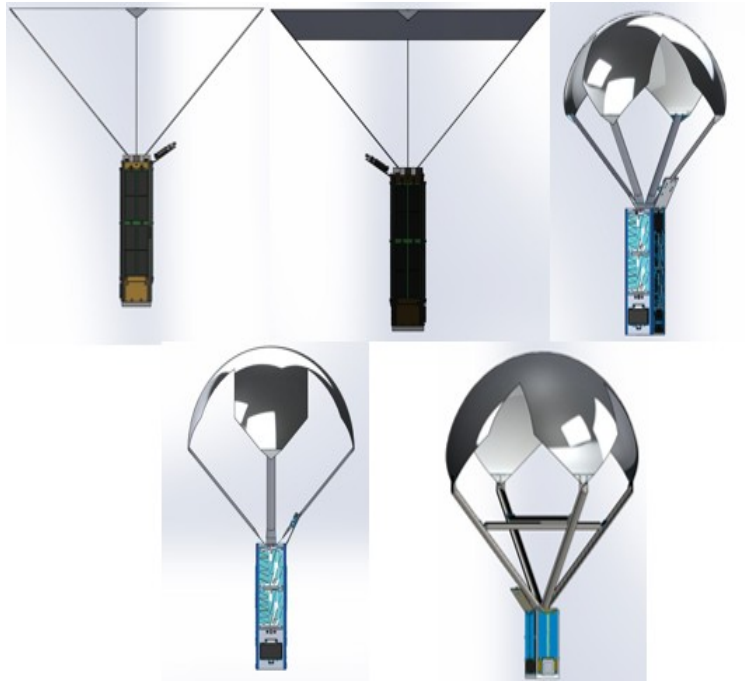


Figure 19: Five Exo-Brake scenarios for various surface areas and configurations [9]

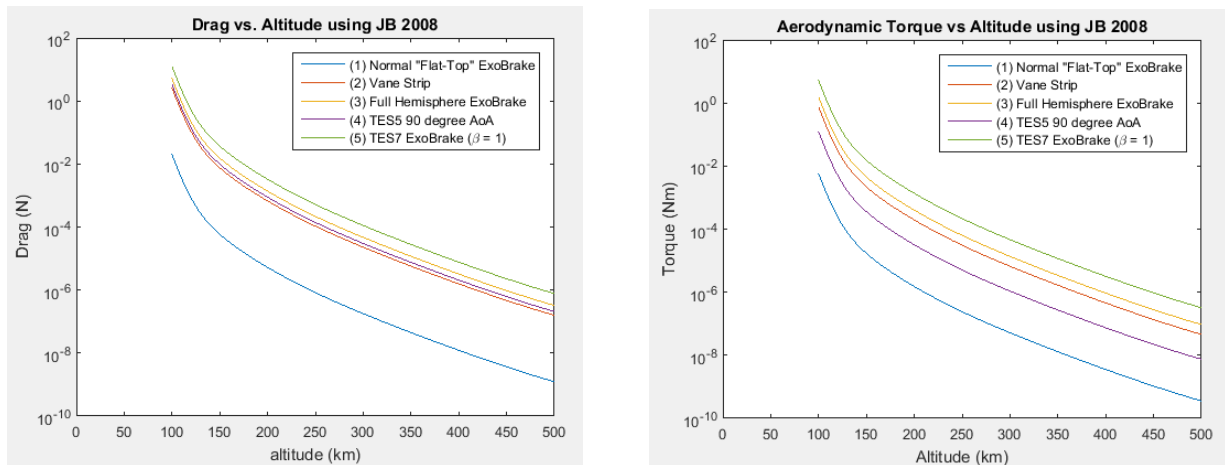


Figure 20: Exo-Brake aerodynamic drag force and torque for various surface areas and configurations

As expected, the Exo-Brake with the highest effective surface area produces the most drag and torque. In order to broadcast via Iridium’s forward pointing patch antenna, the satellite must be pointed in the direction of the velocity vector, a meta-stable orientation for which the satellite was designed for. However, if the satellite gets caught in another meta-stable orientation, communication with the satellite can be lost, resulting in a loss of mission. Thus, the Exo-Brake must have the ability to provide enough torque to overcome the gravity gradient and reorient the cubesat.

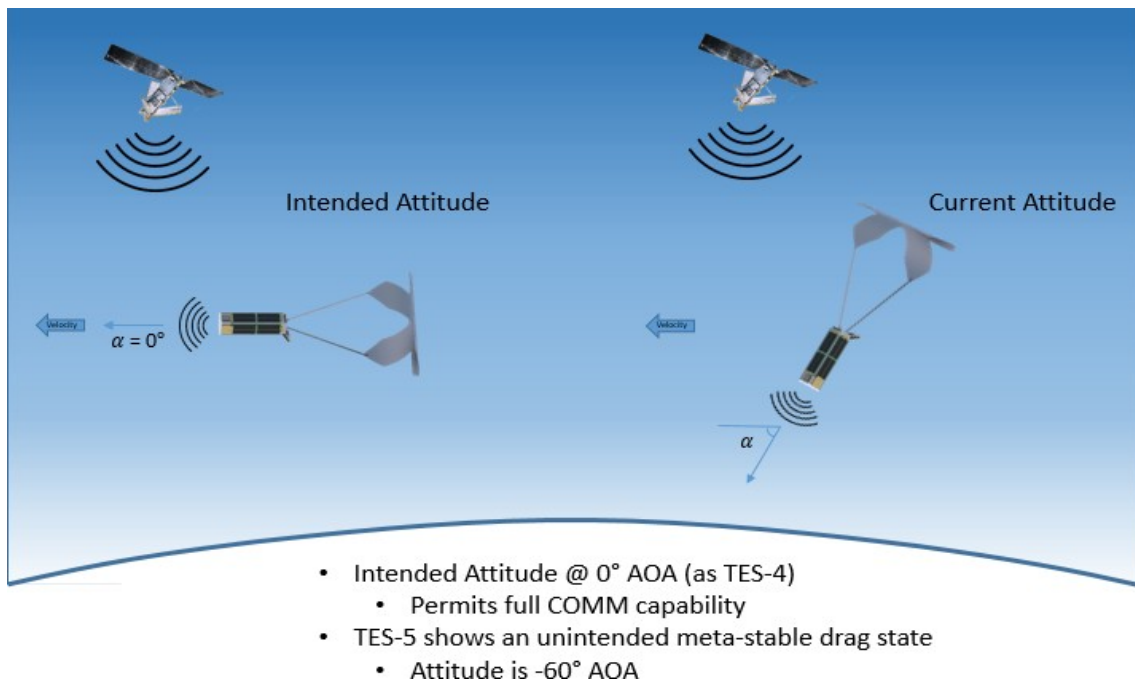


Figure 21: Intended meta-stable orientation for TechEdSat’s forward pointing antenna [9]

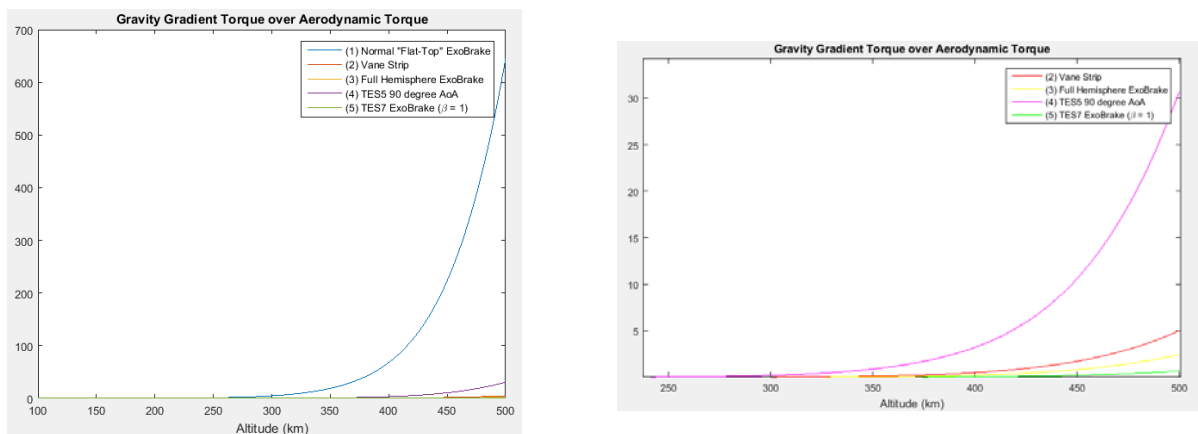


Figure 22: Gravity gradient plotted over aerodynamic torque for various surface areas and configurations

A lower ratio indicates that the aerodynamic torque produced from the Exo-Brake is able to overcome the gravity gradient and reorient the spacecraft while a high ratio suggests that the gravity gradient will dominate and render the Exo-Brake ineffective. Despite the “flat-top” Exo-Brake being ineffective until around 300 km, the other configurations provide significant aerodynamic torque past 400 km. This indicates that at higher altitudes, it may not be possible to perform a handshake, an automated process between the on-board modem and the satellite network that dynamically sets parameters to establish a communication channel. While a secondary antenna mounted on the side of the cubesat would allow additional broadcasting, there is no current method of controlling the cubesats roll orientation, leaving this as an unreliable, yet attractive secondary option if both are integrated into the system. Because TechEdSat is focused on both quick payload returns and controlled de-orbits, a secondary patch antenna is mounted on the side to increase the chances of successful handshakes per orbit.

### 4.3 De-Orbit Propagator

Before re-entry targeting can be achieved, a reference trajectory of a fixed Exo-Brake surface area can be used to better understand the dynamics of the de-orbit process. Building upon the governing equations of motion found the previous sections, a system of first order differential equations can be presented as

$$\dot{x} = \frac{\partial V}{\partial x} = \frac{\mu x}{r^3} \left(1 - J_2 \left(\frac{R_E}{r}\right)^2 \left(5 \frac{z^2}{r^2} - 1\right)\right) - a_{drag,x} \quad (64)$$

$$\dot{y} = \frac{\partial V}{\partial y} = \frac{\mu y}{r^3} \left(1 - J_2 \left(\frac{R_E}{r}\right)^2 \left(5 \frac{z^2}{r^2} - 1\right)\right) - a_{drag,y} \quad (65)$$

$$\dot{z} = \frac{\partial V}{\partial z} = \frac{\mu z}{r^3} \left(1 - J_2 \left(\frac{R_E}{r}\right)^2 \left(5 \frac{z^2}{r^2} - 1\right)\right) - a_{drag,z} \quad (66)$$

where

$$a_{drag,x} = -\frac{C_D A \rho}{m} (\dot{x} + \omega_e x)^2 \quad (67)$$

$$a_{drag,y} = -\frac{C_D A \rho}{m} (\dot{y} - \omega_e y)^2 \quad (68)$$

$$a_{drag,z} = -\frac{C_D A \rho}{m} \dot{z}^2 \quad (69)$$

In order to decrease the computational expense, only three degrees of freedom (3DoF) were utilized compared to the usual six. While fixing the vehicles attitude to an angle of attack and slideslip angle of  $0^\circ$  further constrains the problem, the results are expected to yield accurate estimates due to the theorized lack of large-scale attitude dynamics during an actual flight. Using Matlab's ODE45, a simple ordinary differential equation solver, the position and velocity vectors of the spacecraft can be propagated until an altitude of 150 km is reached. After each timestep, the orbital parameters are recalculated to provide an updated initial condition for the next integration. While other perturbations such as solar radiation pressure, oceanic tides, and additional celestial bodies all contribute to the orbital lifetime of the satellite, the  $J_2$  and atmospheric drag accelerations are the most significant. As previously mentioned, the Jacchia Bowman 2008 atmospheric model was used to generate the density at specified longitudes, latitudes, and altitudes for the given day and year of the mission. Using the beginnings of a source code from the Mathworks website, a function was created inside the differential equation to continuously calculate the appropriate density at the current latitude, longitude, and altitude [7].

The accuracy of this propagator can be validated by recreating test data from TechEdSat 4. Deployed in March 2015, TES4 had a pre-flight estimated ballistic coefficient of  $8 \frac{kg}{m^2}$  in the desired orientation while taking just over 29 days to de-orbit. However, because the satellite

will oscillate around a meta-stable orientation and not remain constant, the ballistic coefficient will vary along with the effective reference area exposed to the flight path. Thus, in order to

accurately capture the satellite's de-orbit trajectory, a ballistic coefficient range of  $7 \pm 2 \frac{kg}{m^2}$  will be used to duplicate the TES4 test data. Despite not having on board inertial measurement units or Global Positioning Systems (GPS), all flight data was retrieved via TLE's and based on ground range estimates taken every couple of days.

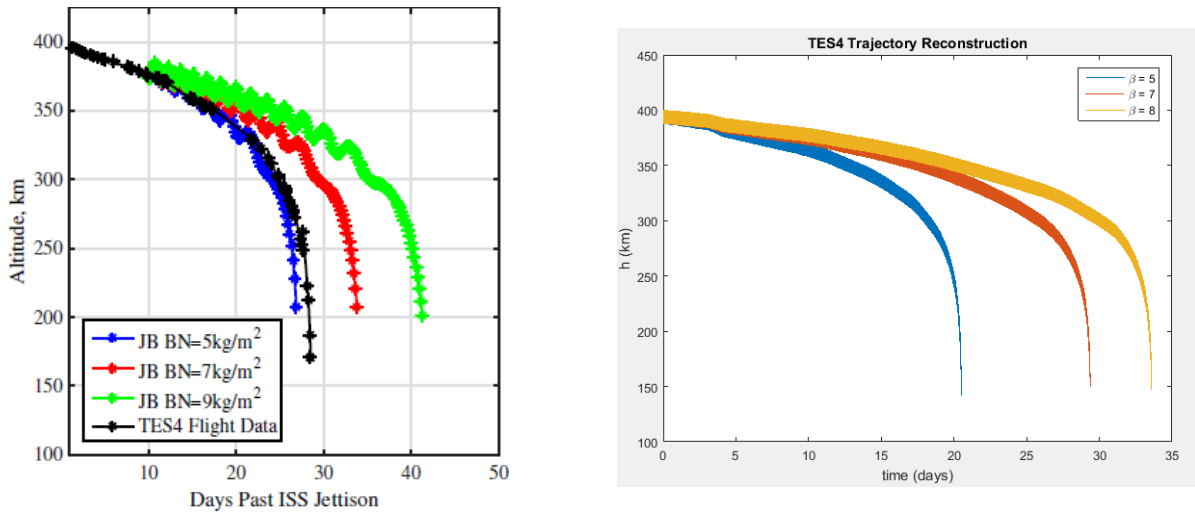


Figure 23: TES4 (2015) trajectory reconstruction comparing POST2 [3] (right) and the current MATLAB propagator

After reconstructing the 2015 TechEdSat 4 mission, a ballistic coefficient of  $7 \frac{kg}{m^2}$  was found to be accurate to within a day of the the actual re-entry time. De-orbiting in just under 30 days, the propagator closely matched the flight data of 29 plus days. Additional tests were run to compensate for the potential ballistic coefficient ranges and give a set of bounds where the satellite would re-enter based off slight angular oscillations.

The possible effectiveness of the Exo-Brake can be tested by running two simulations with a minimum and maximum drag configuration. Under the maximum reference area, the ballistic coefficient approaches  $8 \frac{kg}{m^2}$  compared to a 60 % deployed ballistic coefficient of  $13 \frac{kg}{m^2}$ . Starting on April 10, 2014 at an altitude of 400 km, the fully deployed Exo-Brake re-entered almost 13 days before the partially deployed satellite. Given that the satellite has an orbital period of roughly 90 minutes per orbit, the partially deployed Exo-Brake CubeSat will experience over 200 more orbits, giving the satellite a generous amount of time to target any location within the orbits path.

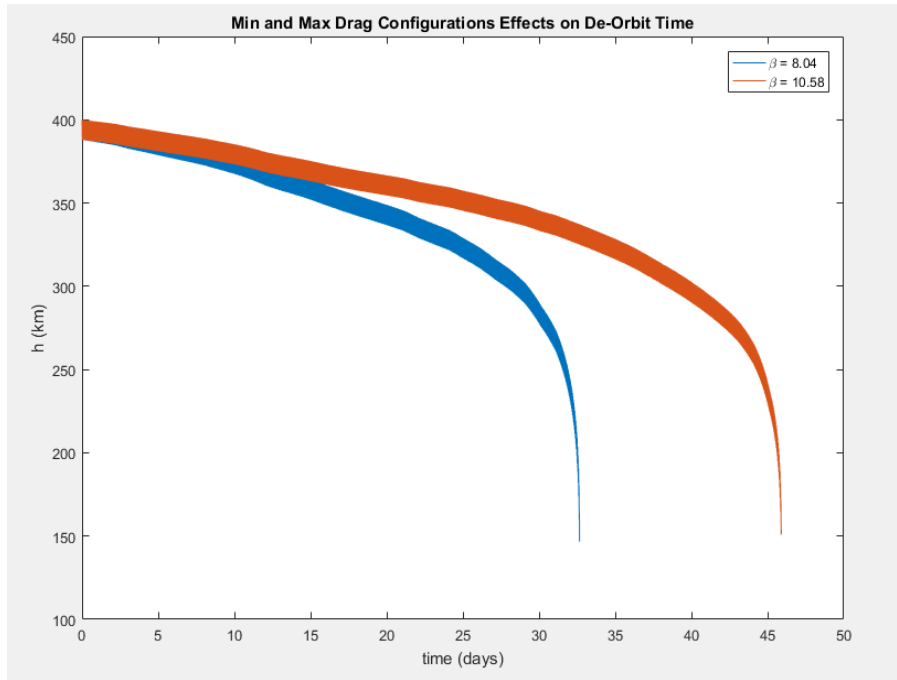


Figure 24: Difference in days to de-orbit for a minimum and maximum Exo-Brake deployment

## 4.4 De-Orbit Targeting Via Aerodynamic Drag

Performing a series of drag modulation maneuvers makes targeting a specific latitude and longitude possible through various optimization algorithms, provided the desired location lies on the initial orbit path. However, due to the limited accuracy of drag modulation, a tolerance of a 100 km radius will be used as a success criteria for point targeting. In addition, the total number of modulations should be minimized as much as possible to lower the risk of mechanical failure. A terminal altitude of 150 km was used to provide additional time for the final stage, a guided parafoil, to safely steer the satellite remains to the target location.

### 4.4.1 Analytically Calculating Re-Entry Location Based on Applied Controls

Using the approach suggested by Sanny Omar and Riccardo Bevilacqua [14], a targeting algorithm of a satellite can be computed by first propagating an initial trajectory and analyzing perturbations from a set of initial conditions. By mapping an initial trajectory to the final impact location, rapid calculation and testing of modulating control parameters can be evaluated until a desired latitude and longitude are obtained. However, before the control algorithm can be discussed, an outline of the effects of orbit perturbations must first be analyzed. Starting from the Gaussian Variation of Parameters equations from Vallado's book [13], the change in semi-major axis can be approximated as follows:

$$\frac{da}{dt} = \frac{2}{n} \sqrt{\frac{p}{1-e^2}} [e \sin \theta F_r + \frac{p}{r} a_{drag}] \quad (70)$$

where the mean motion,

$$n = \sqrt{\frac{\mu}{a^3}} \quad (71)$$

By Simplifying to a circular orbit around a spherical Earth, the new change in semi-major axis with respect to time becomes

$$\frac{da}{dt} = \frac{2a_{drag} \sqrt{a^3}}{\sqrt{\mu}} \quad (72)$$

Substituting the acceleration due to drag, the velocity of a circular orbit, and rearranging to solve for the time derivative results in the following equation:

$$-\frac{\beta da}{2\sqrt{\mu a} \rho} = dt \quad (73)$$

Integrating equation (73) from an initial semi-major axis,  $a_0$ , calculates the total time required for a spacecraft in a circular orbit to reach a final semi-major axis,  $a_f$ .

$$\Delta t = - \int_{a_0}^{a_f} \frac{\beta da}{2\sqrt{\mu a} \rho} \quad (74)$$

If the time required to reach  $a_f$  with a ballistic coefficient of  $\beta_1$ , then the relationship for the time required to reach the same final semi-major axis can be expressed as

$$\Delta t_2 = \frac{\beta_2 \Delta t_1}{\beta_1} \quad (75)$$

In addition, the mean motion for a circular orbit can be expressed as the time rate of change, or true anomaly,  $\theta$ .

$$n = \frac{d\theta}{dt} \quad (76)$$

Multiplying by equation (73) and substituting n with equation (71) results in the following:

$$d\theta = -\frac{\beta da}{2a^2 \rho} \quad (77)$$

Integrating with respect to an initial and final semi-major axis will result in the change in true anomaly over the provided interval.

$$\Delta\theta = - \int_{a_0}^{a_f} \frac{\beta da}{2a^2 \rho} \quad (78)$$

The average orbital angular velocity can then be expressed as the ratio between equation (78) and (74).

$$\omega_{avg} = \frac{\Delta\theta}{\Delta t} \quad (79)$$

Because the effects of zonal harmonics are to be considered, the average rate of change in precession, assuming a circular orbit, can be determined by the following equation:

$$\dot{\Omega}_{avg} = \frac{3 \sqrt{\mu} J_2 R_e^2}{2(1-e^2)a^{7/2}} \cos i \quad (80)$$

If the trajectory has previously been numerically propagated, then  $\dot{\Omega}_{avg}$  can be calculated by dividing the total change in right ascension by the total change in time. If given  $\dot{\Omega}_{avg}$ , then the total change in right ascension can be approximated by

$$\Delta\Omega = \dot{\Omega}_{avg}\Delta t \quad (81)$$

The initial trajectory is propagated using initial conditions with a predetermined ballistic coefficient,  $\beta_{10}$  until  $t_{s,old}$ , the initial time until swapping to  $\beta_{20}$ , and is propagated until the final semi-major axis is reached. This is called the terminal point, which can be characterized by the change in time,  $\Delta t_{term}$ , the change in true anomaly,  $\Delta\theta_{term}$ , and the change in right ascension,  $\Delta\Omega_{term}$ . The new terminal point location is then analytically determined for each set of control parameters at this point to estimate the new de-orbit location based off the updated  $\Delta\theta_{term}$  and  $\Delta\Omega_{term}$  variables. The location of the terminal point required to target a specified de-orbit location can then be uniquely determined based off the approximations that the orbits inclination does not change significantly due to environmental perturbations and that  $\Delta\theta_{term}$ ,  $\Delta\Omega_{term}$ , and  $\Delta t$  are approximately the same for each new trajectory. The purpose of the targeting algorithm then becomes to define a new trajectory which passes through the terminal point that guarantees a re-entry at the desired latitude and longitude. During the initial propagation, the time, position, velocity, and average orbital angular velocity at each step are recorded from the initial time,  $t_0$ , to the current time,  $t$ , and from the current time to the terminal time,  $t_{term}$ . However, one previous assumption made was that the argument of perigee would not change between the initial and final orbits. While this is not particularly true, the argument of perigee can be approximated by utilizing the mean longitude, the point at which an orbiting body could be found if its orbit were circular and perturbation free.

$$\lambda = \Omega + \omega + M_e \quad (82)$$

where,

$$M_e = E - e \sin E \quad (83)$$

$$E = 2 \tan^{-1} \left( \frac{1-e}{1+e} \tan \frac{\theta}{2} \right) \quad (84)$$

Mathematically, the mean longitude is the angular distance the body would have from the reference direction if it were to move at a uniform speed. Because the mean longitude increases uniformly with time, the mean longitude at future point can be described as

$$\lambda = \lambda_0 + n(t - t_0) \quad (85)$$

where  $\lambda_0$  is the mean longitude at epoch,  $n$  is the rate of motion in mean longitude, and  $t_0$  is the time at epoch. Similarly, the mean motion at a future point can be equated as

$$M = M_0 + n(t - t_0) \quad (86)$$

$$\text{where } M_0 = \lambda_0 - (\Omega_0 + \omega_0) \quad (87)$$

$$n = n - (\Omega - \omega) \quad (88)$$

The terminal location of the spacecraft can be calculated from equations (75), (79), and (81) using the same initial conditions and varying ballistic coefficients,  $\beta_1$  and  $\beta_2$ , and the time until these ballistic coefficients are swapped ( $t_s$ ). Determining the terminal point can then be broken down into three different phases, each with respect to an initial and final semi-major axis with the same ballistic coefficients between  $a_0$  and  $a_f$ . By keeping the ballistic coefficients constant for the given semi-major axis intervals, the change in orbital elements for each new trajectory can be observed for each phase. The following figure represents both the old and new trajectories for varying  $t_s$ , or the time when  $\beta_1$  swaps to  $\beta_2$ .

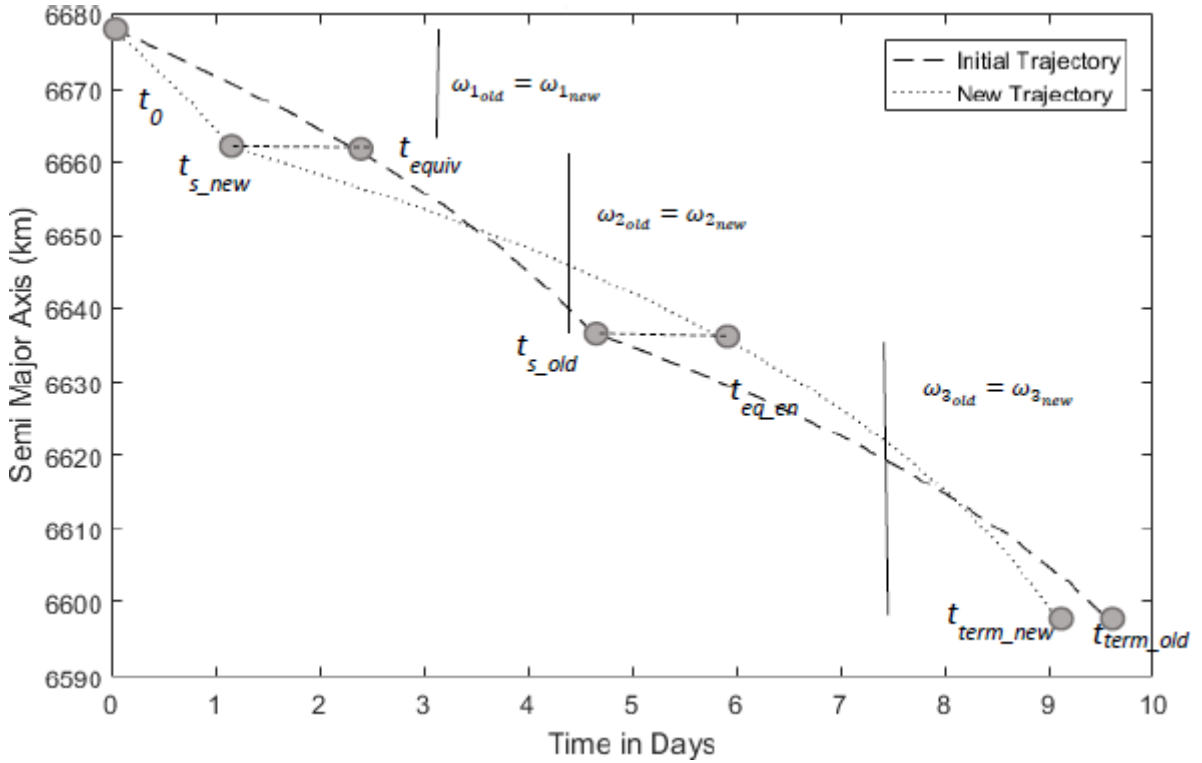


Figure 25: Semi-major axis over time for both initial and new trajectories [14]

In this particular case,  $t_{equiv}$  is less than  $t_{s,old}$ , effectively lowering the time until  $a_f$  is reached. Assuming that the only orbital elements changing are  $\theta$ ,  $a$ , and  $\Omega$ , the total time and orbital elements at de-orbit can be calculated and converted to the ECI and LLA (latitude, longitude, altitude) frames for the final de-orbit latitude and longitude. Once this analytical relationship between the initial conditions and the final latitude and longitude is established, the effects of drag modulation can be analyzed for point targeting.

Using the analytical mapping between the control parameters ( $\beta_1$ ,  $\beta_2$ , and  $t_s$ ) and the de-orbit latitude and longitude, the desired trajectory can be analytically calculated and decoupled from the corresponding drag modulations required to achieve point targeting. Assuming that the desired target is below the orbits inclination and that the ballistic coefficient is modulated

( $\beta_1$  and  $\beta_2$  are not equal), any location is possible to target given sufficient initial altitude and ExoBrake surface area.

The change in true anomaly required for latitude targeting can be calculated by taking the modulus of the difference between the initial and final angles.

$$\Delta\theta_d = \text{mod}(\varphi_d - \varphi_i, 2\pi) \quad (89)$$

where  $\varphi_i$  is the initial angle and  $\varphi_d$  is the final, desired angle. Analytically calculating  $\Delta\theta_d$  to get an increase in swap time necessary to produce a desired  $\Delta\theta_d$  can be done by analyzing the latitude controllability. Controllability is the ability to bring an initial state to a desired final state in a finite amount of time from a given set of control parameters. If the system is not controllable, then the satellite will be unable to reach the targeted latitude or longitude. Parameters such as an insufficient initial altitude or too small of a drag configuration variation can lead to inaccurate control of the spacecraft. Latitudinal controllability can be achieved by first looking at the effects of only varying  $t_s$  from an initial trajectory. Considering scenario in which the time of swapping ballistic coefficients is increased, the second phase of the new trajectory will have a different change in time and true anomaly from the old as shown in the following figure.

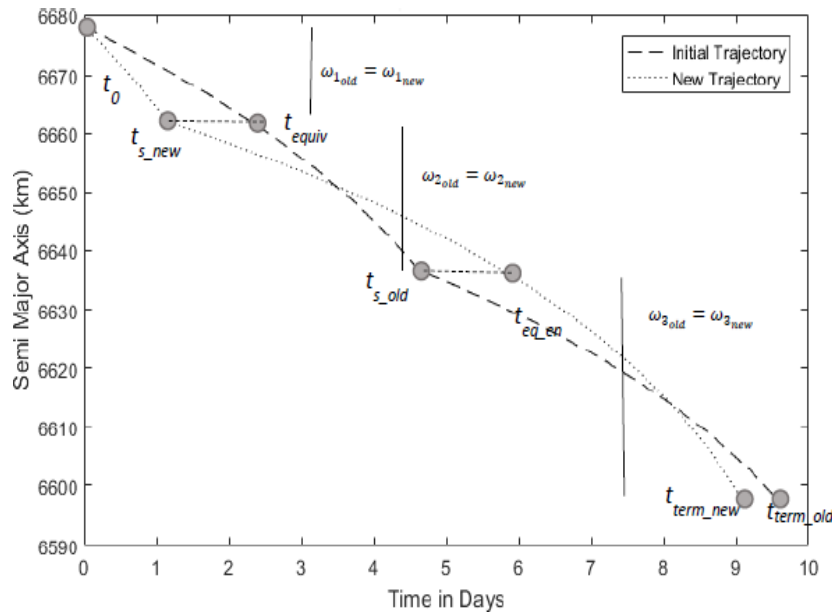


Figure 26: The effects of an increase in swap time with respect to time in days [14]

If the time required for the second phase is  $\Delta t_{20}$ , then the time required for phase two in the new trajectory can be calculated as

$$\Delta t_2 = \frac{\beta_1 \Delta t_{20}}{\beta_2} \quad (90)$$

given that the semi-major axis interval and the ballistic coefficients do not vary. The total increase in time caused from the increase in  $t_s$  is equal to the difference in change of swap time

and the time required for phase two of the initial trajectory. Combined with equation (90), the difference in orbital lifetime between new and old trajectories can be rearranged as

$$\Delta t_d = \Delta t_s \left(1 - \frac{\beta_2}{\beta_1}\right) \quad (91)$$

If  $\beta_1$  is greater than  $\beta_2$ , then the orbital lifetime of the spacecraft will decrease given an increase in  $t_s$  due to the decrease in drag. Inversely, if the ballistic coefficient decreases after a decrease in  $t_s$ , then the change in swap time would be equal to the negative time required for phase two of the initial trajectory. The difference in total true anomaly change can then be calculated once the change in orbital lifetime is determined as

$$\Delta \theta_d = \omega_{2,avg} \Delta t_d \quad (92)$$

where  $\omega_{2,avg}$  is the average angular velocity calculated during the second phase from the initial trajectory. This is valid because all of the orbital lifetime variations and changes in true anomaly occur in this phase. However, there is a maximum time for which the change in ballistic coefficients can take place. If  $t_s$  is set to its maximum value, then the ballistic coefficient will not change until the terminal point is reached. The maximum time can then be written as

$$t_{s,max} = t_{s,old} + (t_{term,old} - t_{s,old}) \frac{\beta_1}{\beta_2} \quad (93)$$

While the latitude targeting algorithm must select a  $t_s$  value less than the maximum, it is important to enforce additional constraints due to longitudinal controllability being limited by times farther away from the middle of the attainable range. Therefore, only  $t_s$  values between 25% and 75% of the maximum will be used as valid swap times.

When calculating the optimal swap time for latitude targeting, a sweep of possible swap times can be performed to better understand its effects on the terminal location. As shown in the following figure, a wide range of locations can be targeted just from varying the swap time.

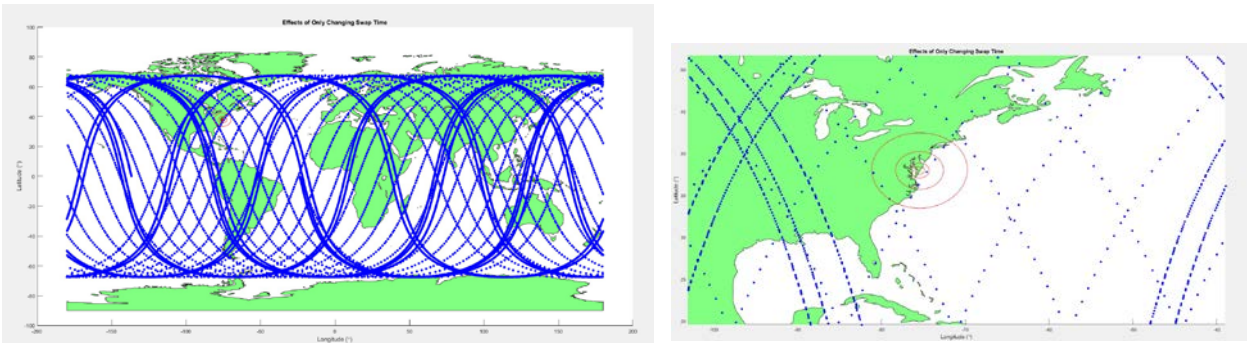


Figure 27: Possible terminal locations from varying only the swap time

In order to determine the optimal swap time, a for refined search of the latitude error can be conducted. Every time the latitude error, actual latitude minus the target latitude, has a

sign change, somewhere between the two points yields the correct latitude its corresponding swap time. A simple algorithm was constructed to look at all possible points within a  $\pm$  of  $10^\circ$  that underwent a sign change.

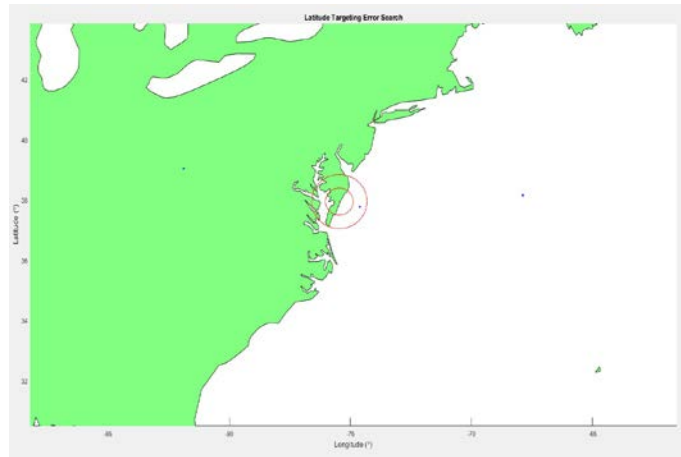


Figure 28: Sign Changes in swap times used to refine latitude targeting

From these potential swap times, and expanded search can be conducted to determine the time the latitude error becomes zero. However, because the onboard hardware will not be able to effectively implement winch controls in fractions of seconds, the minimum latitude error was selected from one second intervals.

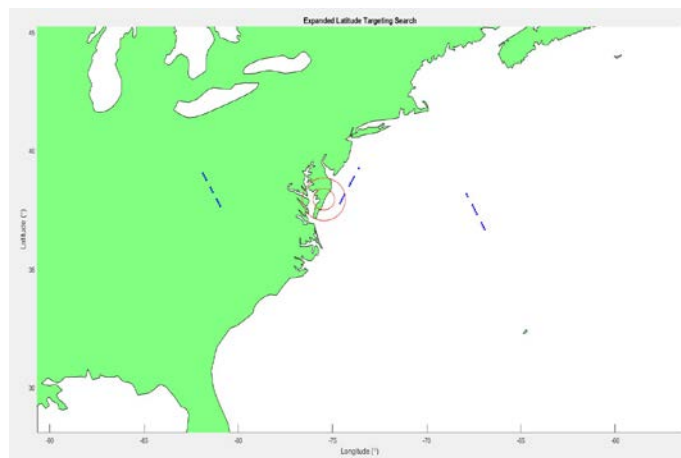


Figure 29: An expanded latitude search to determine the minimal latitude targeting error

When choosing the optimal swap time, the value that yields the minimum positive longitude error must be chosen. A positive longitude error indicates that the satellites orbit must last slightly longer with the same total change in true anomaly to hit the desired target longitude while a negative error would have to last slightly shorter. Positive longitude errors are desirable because the initial control parameters are designed to make the orbit last longer without changing the total change in true anomaly.

Once the best possible  $t_s$  time is determined, the initial and final ballistic coefficients must be varied to eliminate the longitudinal error without disrupting the total change in true anomaly.

The effects of modulating ballistic coefficients on impact location, assuming the drag configurations are swapped at the same semi-major axis in both the new and old configurations, can be calculated as

$$\Delta\theta_1 + \Delta\theta_2 = \Delta\theta_t \quad (94)$$

$$\Delta t_1 + \Delta t_2 = \Delta t_t \quad (95)$$

$$\Delta\theta_1 = \frac{\Delta\theta_{10}\beta_1}{\beta_{10}} \quad (96)$$

$$\Delta\theta_2 = \frac{\Delta\theta_{20}\beta_2}{\beta_{20}} \quad (97)$$

$$\Delta t_1 = \frac{\Delta t_{10}\beta_1}{\beta_{20}} \quad (98)$$

$$\Delta t_2 = \frac{t_{20}\beta_2}{\beta_{20}} \quad (99)$$

where  $\Delta t_t$  is the total time the new trajectory takes to reach the terminal point,  $\Delta t_i$  is the time until swap point in the new respective trajectory, and  $\Delta\theta_t$  is the desired total change in true anomaly of the new trajectory until the terminal point is reached. Using equations (94) - (99),  $\beta_1$  and  $\beta_2$  can be rearranged to analytically calculate the desired  $\Delta\theta_t$  and  $\Delta t_t$ .

$$\Delta\theta_t = \Delta\theta_1 + \Delta\theta_2 = \frac{\Delta\theta_{10}\beta_1}{\beta_{10}} + \frac{\Delta\theta_{20}\beta_2}{\beta_{20}} \quad (100)$$

$$\beta_1 = \frac{\Delta\theta_t}{\beta_{10}\beta_2 \left( \frac{\Delta\theta_t}{\beta_2} - \frac{\Delta\theta_{20}}{\beta_{20}} \right)} \quad (101)$$

$$\Delta t_t = \frac{\Delta t_{10}\beta_1}{\beta_{10}} + \frac{\Delta t_{20}\beta_2}{\beta_{20}} \quad (102)$$

$$\beta_2 = \frac{\beta_{20}(\Delta t_t \Delta\theta_{10} - \Delta t_{10} \Delta\theta_t)}{\Delta t_{20} \Delta\theta_{10} - \Delta t_{10} \Delta\theta_{20}} \quad (103)$$

Here,  $\Delta\theta_t$  will be the same as it is in the  $t_s$  trajectory calculated from the latitude targeting while the time to de-orbit and total change in true anomaly of the updated trajectory after the terminal point will be identical to the initial trajectory after the drag profile is manipulated by the targeting algorithm. Assuming the the swap times occur at the same semi-major axis for the new and initial trajectories, it becomes important to update the new swap time,  $t_{s,new}$

$$t_{s,new} = \frac{t_{s,old}\beta_1}{\beta_{10}} \quad (104)$$

When optimizing the longitude error, a similar search to the latitude targeting algorithm can be performed. By varying the total time the new trajectory takes to reach the terminal point, the possible terminal locations can be shown as follows.

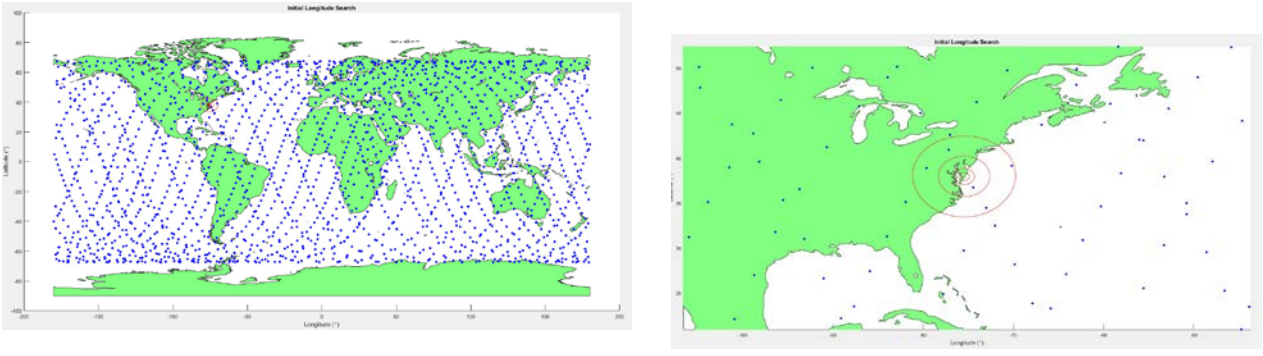


Figure 30: Possible terminal locations from varying  $\Delta t$

As in the latitude targeting algorithm, the optimal  $\Delta t$  can be determined by looking at the sign changes in longitude error and expanding the search at one second intervals.

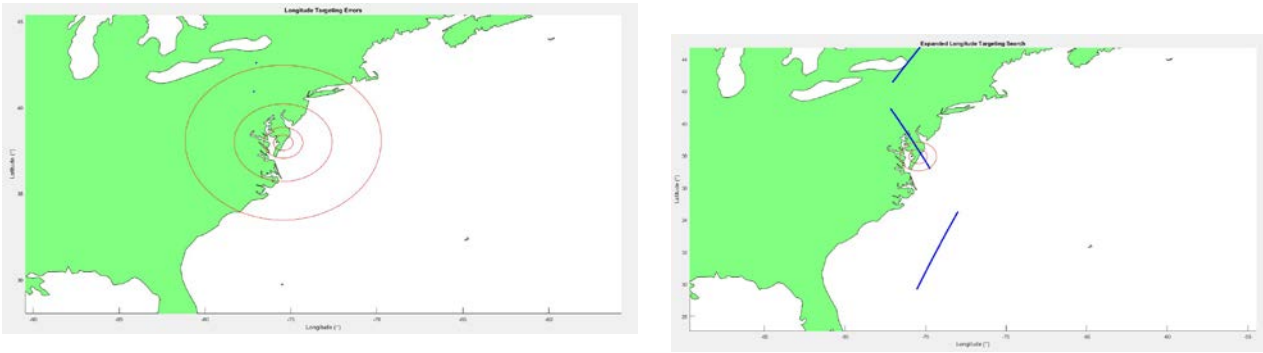


Figure 31: Expanded search for possible terminal locations by varying  $\Delta t$

Given a specific  $\beta_2$ ,  $\beta_1$  must be calculated to ensure the difference in total change in true anomaly between the initial and final trajectories. If, for example, the ballistic coefficient is increased at the swap time by decreasing the reference area, then the orbital lifetime will decrease due to the increase in drag. With the change in true anomaly calculated for the different phases for the new trajectory, the true anomaly at the terminal location can be calculated using the mean motion of the spacecraft and the change in true anomaly of the initial trajectory. Using the relation between true anomaly, angular velocity, and time, the average mean motion of the initial trajectories second phase can be calculated:

$$n_{2,avg} = \frac{\theta_{20} - \theta_{10}}{t_2} \quad \left( \frac{\text{rad}}{\text{s}} \right) \quad (105)$$

Because the spacecraft will have the same ballistic coefficients for phase two of the initial trajectory, and the final phase of the new trajectory, the only differences will be the amount of time and the true anomaly at the terminal location.

$$n_{2,avg} = \frac{\theta_3 - \theta_2}{t_3} \quad \left( \frac{\text{rad}}{\text{s}} \right) \quad (106)$$

Rearranging the equation solves for theta, which can then be used as one of the final orbital elements to compute the position and velocity vector. Using the known variables at both

epoch and the terminal location, the final argument of perigee can be calculated. From here, calculating the position and velocity vectors become trivial once all of the orbital elements are known. Using algorithm 4.2 from Curtis's book, the following pseudo code can be used to compute the position and velocity vectors at the terminal location.

1. Calculate the distance

$$r = \sqrt{\mathbf{r} \cdot \mathbf{r}} \quad (107)$$

2. Calculate the speed

$$v = \sqrt{\mathbf{v} \cdot \mathbf{v}} \quad (108)$$

3. Calculate the radial velocity

$$v_r = \mathbf{r} \cdot \frac{\mathbf{v}}{r} \quad (109)$$

4. Calculate the specific angular momentum:

$$\mathbf{h} = \mathbf{r} \times \mathbf{v} \quad (110)$$

5. Calculate the magnitude of the specific angular momentum

$$h = \sqrt{\mathbf{h} \cdot \mathbf{h}} \quad (111)$$

6. Calculate the inclination

$$i = \cos^{-1} \left( \frac{h_z}{h} \right) \quad (112)$$

7. Calculate the node line

$$\mathbf{N} = [0 \ 0 \ 1] \times \mathbf{h} \quad (113)$$

8. Calculate the magnitude of  $\mathbf{N}$

$$N = \sqrt{\mathbf{N} \cdot \mathbf{N}} \quad (114)$$

9. Calculate the right ascension of the ascending node

$$\Omega = \begin{cases} \cos^{-1} \frac{N_x}{N} & (N_y \geq 0) \\ 2\pi - \cos^{-1} \frac{N_x}{N} & (N_y < 0) \end{cases} \quad (115)$$

10. Calculate the eccentricity vector

$$\mathbf{e} = \frac{1}{\mu} \mathbf{v} \times \mathbf{h} - \mu \frac{\mathbf{r}}{r} = \frac{1}{\mu} r v^2 - \mathbf{v}(\mathbf{r} \cdot \mathbf{v}) - \mu \frac{\mathbf{r}}{r} \quad (116)$$

11. Calculate the eccentricity

$$e = \sqrt{\mathbf{e} \cdot \mathbf{e}} \quad (117)$$

12. Calculate the argument of perigee

$$\omega = \begin{cases} \cos^{-1} \left( \frac{\mathbf{N} \cdot \mathbf{e}}{N e} \right) & (\mathbf{e} \cdot \mathbf{z} \geq 0) \\ 2\pi - \cos^{-1} \left( \frac{\mathbf{N} \cdot \mathbf{e}}{N e} \right) & (\mathbf{e} \cdot \mathbf{z} < 0) \end{cases} \quad (118)$$

13. Calculate the true anomaly

$$\theta = \begin{cases} \cos^{-1} \left( \frac{\mathbf{e} \cdot \mathbf{r}}{e r} \right) & (v_r \geq 0) \\ 2\pi - \cos^{-1} \left( \frac{\mathbf{e} \cdot \mathbf{r}}{e r} \right) & (v_r < 0) \end{cases} \quad (119)$$

Once the position and velocity vectors are known, they can be converted from the ECI reference frame to a latitude, longitude, and altitude (LLA) coordinate system by first rotating to the earth-centered inertial frame (ECEF). The earth-centered inertial frame is a geographical coordinate system with its center located at the center of mass of the earth. Its axis are fixed with respect to the surface of the earth and does not rotate about the z-axis like the earth-centered internal frame. From the ECEF frame, the latitude, longitude, and altitude of a given position vector can be computed with paired with a time stamp in the universal time coordinated (UTC) format.

This targeting algorithm aims to find the optimal set of control parameters resulting in a minimized latitude and longitude targeting error. After the optimal control parameters are found, the initial trajectory can then be run with the new  $t_s$ ,  $\beta_1$ , and  $\beta_2$  values. While there may be some error between the propagated trajectory and the analytical solution due to assumptions and unmodeled parameters, both will converge within a certain tolerance after a few iterations. However, one of the biggest flaws in the analytical calculations was using an exponential atmospheric model to generate density values. Despite decreasing complexity, the accuracy of analytical perturbations suffer from this approximation. In addition, the MATLAB propagation simulation took around 15 minutes to run, making it unattractive to run on-board a CubeSat without first converting to C and optimizing. However, if run every few orbits to continuously update the numerical propagation and coupled with a feedback loop, the targeting algorithm can be used to guide the satellite to within 100 km of the target.

## 5 Results

In order to test the effectiveness of the ExoBrake's ability to target, several simulations were run at random potential deployment locations from an altitude of 300 km. The intended target, NASA Wallops, was chosen as a targeting location due to their satellite tracking capabilities necessary to help validate future TechEdSat experiments. The final swap time's and total

targeting error's were recorded as follows:

| Initial Orbital Parameters<br>( $a$ (km), $e$ , $\Omega$ (deg), $\omega$<br>(deg), $\theta$ (deg), $i$ (deg)) | Final Swap Time (sec) | Targeting Error (km) |
|---|-----------------------|----------------------|
| (6678.55, 0, 67.529, 58.417,<br>0, 40.757)  | 254832                | 21.39                |
| (6672, .00029, 51.641,<br>244.3, 220.82, 139.273)   | 121260                | 37.233               |
| (6678.58, .0245, 57.69,<br>306.615, 314.19, 99.89)  | 103442                | 102.03               |
| (6678.55, 0.00035, 54.49,<br>201.01, 269.01, 80.99)   | 128550                | 31.1322              |
| (6678.55, 0.01, 56.29,<br>224.35, 278.599, 270.21)  | 106920                | 17.6835              |

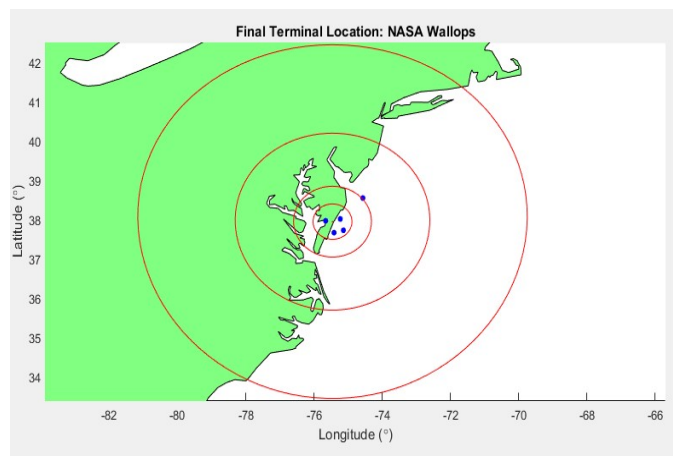


Figure 32: Final terminal locations from 5 randomly selected potential deployments

As shown in the figure about, all but one of the simulations yielded a targeting error under the desired 100 km. In some cases, the varying of swap time alone was enough to maneuver the satellite to within 50 km of the targeted terminal location. While these results determine it is possible to target a location within 100 km, further tests should be run to validate the accuracy and robustness of the algorithm before future flight use.

## 6 Limitations

Due to forces such as atmospheric drag,  $J_2$  perturbations, and gravitational forces from other planets or masses, an initially circular orbit around Earth will not remain perfectly circular, causing the velocity and altitude to increasingly oscillate as the spacecraft de-orbits and the drag forces increase. The aerodynamic drag force slightly reduces the instantaneous velocity of the initially circular orbit, causing the current point to become the orbits apogee. At the perigee, the altitude will be lower while the density is higher, causing a higher velocity and drag force when compared to the apogee. This then converts the old perigee into the new apogee, creating a cycle which explains the oscillations in velocity with respect to altitude. As shown

in the figure below, the oscillations become greater the closer to Earth the spacecraft gets due to the increase in drag.

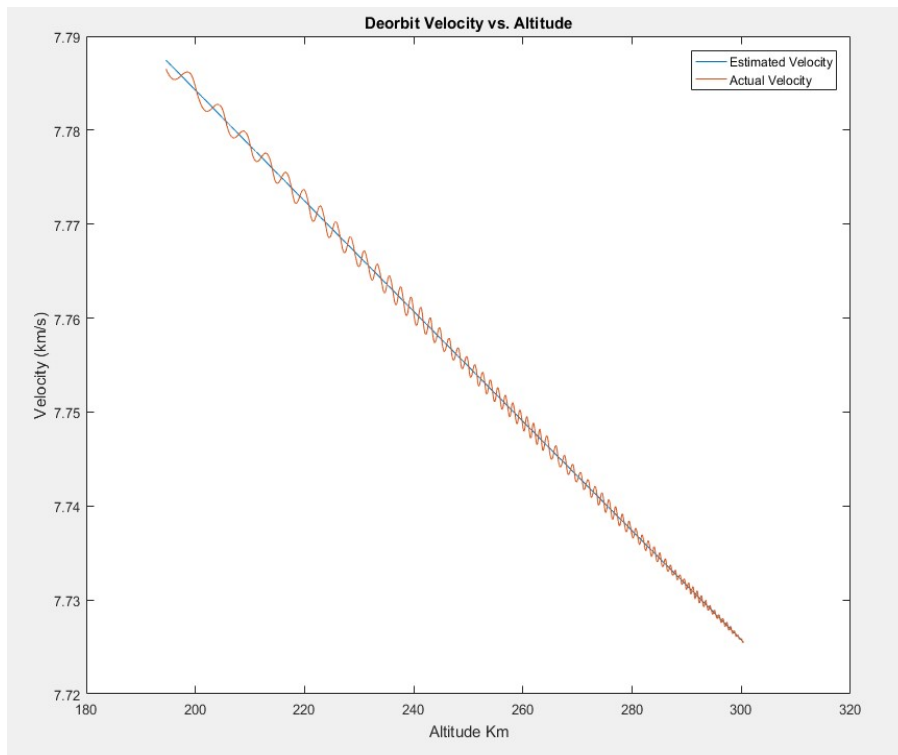


Figure 33: Velocity oscillations over time during an orbit decay

Despite these oscillations being small, the velocity, density, and aerodynamic drag profiles will differ from what they would be for a circular orbit and accumulate small errors over time in the analytically perturbation analysis used to predict the new orbit. However, because the targeting algorithm is based off perturbations from a numerically propagated trajectory using a sophisticated density model, the drag force deviations from the circular orbit will be visible in the numerical calculation.

In addition, a single drag modulation maneuver would not be feasible due to the unknown changes in density or attitude of the spacecraft. One major assumption used in this simulation stated that the spacecraft would remain in its highest drag form throughout the trajectory. While this is true for most of the spacecraft's life, the ExoBrake might not be fully effective at higher altitudes if the aerodynamic torque

## 7 Future Work

While this targeting method proves that the Exo-Brake can successfully guide the satellite to a targeted location provided enough time and inclination in the initial orbit, a single drag modulation will not be enough to account for unknown perturbations when predicting unknown variables such as density or drag. As all simulations were run with preexisting information on solar and geomagnetic indices, these unknown perturbations were accounted for, thus making the simulation provide accurate results with a single maneuver. For this reason, a closed loop

solution will be implemented to ensure that the satellite follows the provided trajectory to ensure the target location is achieved. One such solution is to break the control algorithm into two distinct stages, thus allowing more optimal trajectory tracking without implementing a high amount of drag modulations. The first stage would consist of the single swap maneuver discussed in this paper until a target location at 200 km is reached. This 200 km location will be determined to guarantee that the satellite will be within a window capable of reaching the desired impact location while de-orbiting the satellite in a timely manner.

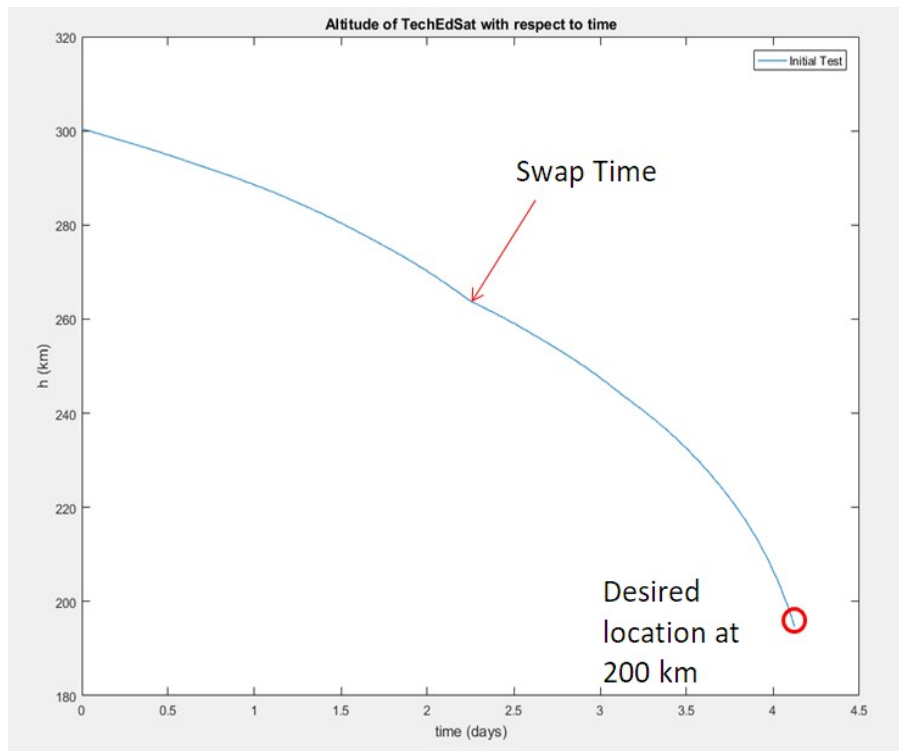


Figure 34: Stage 1 of proposed targeting algorithm

By limiting the number of drag modulations, the risk of failure in the Exo-Brake and winch system is lowered, thus making the control algorithm safer compared to a continuously modulating system. However, as stated before, small perturbations in the density will cause this method to accumulate errors over time without closing the loop. The second stage, beginning once the satellite reaches the 200 km mark, will close the feedback loop and allow the satellite to adjust its deployment configuration on the fly.

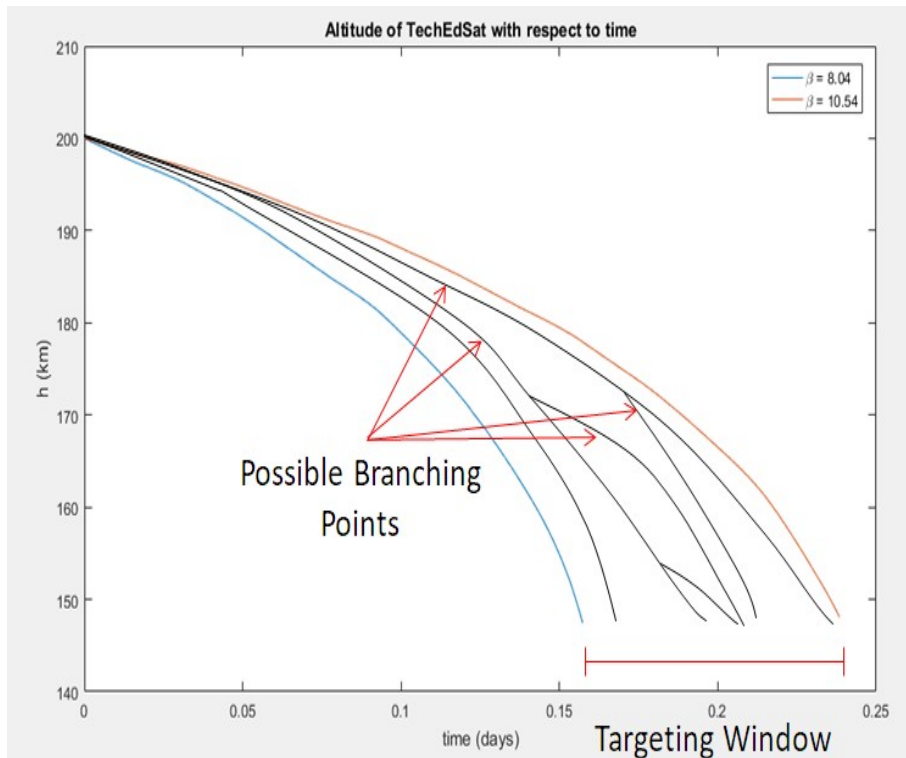


Figure 35: Stage 2 of proposed targeting algorithm

The starting point of stage two creates a window of opportunity based off the minimum and maximum ballistic coefficients. Any further drag modulation combinations would create a new branching point, as shown in the figure above. A closed feedback loop would lie within the targeting window, allowing for the satellite to adjust its ballistic coefficient on the fly to ensure the impact location is reached. This adaptive control method will help compensate for the changes in orbital elements as well as density and drag variables.

Once the second stage of the proposed targeting algorithm is completed, the second stage of SOAREX, a future testbed for the ExoBrake, will utilize a re-entry vehicle called the TDRV (Tube Deployed Re-entry Vehicle) to protect the satellites internal components during the re-entry process. Once re-entry is complete, a guided parafoil will be used to steer the satellite remains to the desired location.

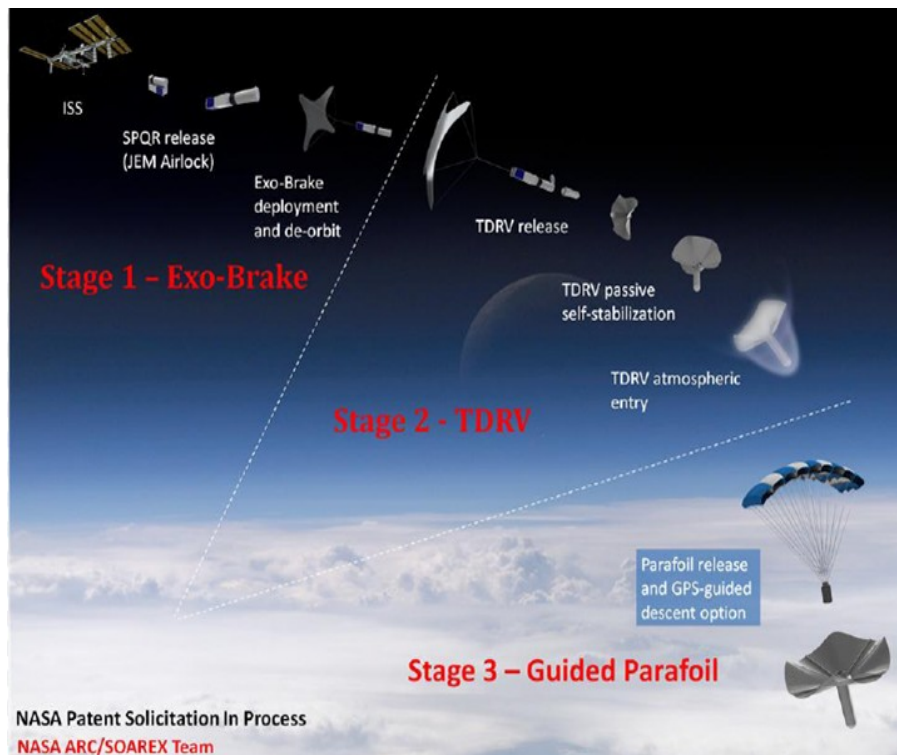


Figure 36: SOAREX Deployment Process proposed to work with the de-orbit targeting algorithm

In order to run the propagator and control algorithm onboard the satellite, the code must also be optimized and converted to C++ to decrease the run time and computational expense of the model. Optimizing the numerical propagation will allow the trajectory to be updated every few days, helping decrease the error accumulation seen in the first stage of the proposed algorithm. Including higher order accuracy conditions such as lunar gravitational and solar pressure effects can also be added to increase the numerical calculations accuracy at the cost of longer convergence times. However, because the de-orbit process is relatively slow, additional computation time can be tolerated so long as the spacecraft can supply the increase in power consumption.

## 8 Conclusions

Using drag modulation, it is possible to guide a CubeSat or small satellite to any location on the globe, provided there is enough time and inclination of the initial orbit. By first numerically propagating the trajectory using an advanced atmospheric model, analytical perturbations can be performed based off simplified assumptions to predict when and where the satellite will reach its terminal location, or a desired altitude of 150 km. This can be used to safely guide satellites and small payloads from the ISS to within 100 km of a desired location at an increased rate without endangering the population. Once the terminal location is reached, the proposed SOAREX stages will be implemented for the re-entry and guided parafoil portion of the trajectory. While further investigation of the targeting algorithm will be performed

to perfect the maneuver through a multi-stage approach, drag modulation can be seen as an attractive and inexpensive alternative to propulsion systems for small satellite recovery.

## References

- [1] Bruce R. Bowman and W. Kent Tobiska. "A New Empirical Thermospheric Density Model JB2008 Using New Solar and Geomagnetic Indices". In: *AIAA* (2008).
- [2] Howard D. Curtis. *Orbital Mechanics for Engineering Students*. 225 Wyman Street, Waltham, 02451, USA: Elsevier Ltd., 2014.
- [3] Soumyo Dutta et al. "Guidance Scheme for Modulation of Drag Devices to Enable Return from Low Earth Orbit". In: *AIAA* (2016).
- [4] E.M. Gaposchkin and A.J. Coster. "Analysis of Satellite Drag". In: *The Lincoln Laboratory Journal* 1.2 (1988).
- [5] E.M. Gaposchkin and A.J. Coster. "Linearized Equations for J2 Perturbed Motion Relative to an Elliptical Orbit". In: *SJSU Master's Thesis and Graduation Research Department of Mechanical and Aerospace Engineering* (2005).
- [6] Maj Edward P. Chatters IV and Maj Bryan Eberhardt and Maj Michael S. Warner. "Orbital Mechanics". In: (2010), pp. 89–114.
- [7] Meysam Mahooti. *Jacchia-Bowman Atmospheric Model*. 2016.
- [8] Gustavo A. Mansilla. "Solar Cycle and Seasonal Distribution of Geomagnetic Storms with Sudden Commencement". In: *Earth Science Research* 3.1 (2014).
- [9] M. Murbach, F. Tanner, and S. Smith. *T5 Mission Anomaly Analysis*. NASA Ames Research Center. 2017.
- [10] NASA. *Guidance and Navigation for Entry Vehicles*. National Aeronautics and Space Administration, 1968.
- [11] Sanny R. Omar and Riccardo Bevilacqua. "Spacecraft De-Orbit Point Targeting using Aerodynamic Drag". In: *AIAA Guidance, Navigation, and Control Conference* (2017).
- [12] Prasenjit Sengupta. "Satellite Relative Motion Propagation and Control in the Presence of J2 Perturbations". In: *Office of Graduate Studies of Texas AM University* (2003).
- [13] D.A. Vallado. *Fundamentals of Astrodynamics and Applications*. Springer-Verlag New York, 2007.
- [14] David A. Vallado and David Finkleman. "A Critical Assessment of Satellite Drag and Atmospheric Density Modeling". In: *AIAA/AAS Astrodynamics Specialist Conference and Exhibit* (2008).
- [15] Josep Virgili, Peter C. Roberts, and Nathan C. Hara. "Atmospheric Interface Reentry Point Targeting Using Aerodynamic Drag Control". In: *Journal of Guidance, Control, and Dynamics* 38.3 (2015).